HHS Public Access

Author manuscript

ACS Nano. Author manuscript; available in PMC 2019 November 27.

Published in final edited form as:

ACS Nano. 2018 November 27; 12(11): 10817–10832. doi:10.1021/acsnano.8b02587.

Tumor Cell-Derived Extracellular Vesicle-Coated Nanocarriers: An Efficient Theranostic Platform for the Cancer-Specific Delivery of Anti-miR-21 and Imaging Agents

Rajendran JC Bose[†,‡], **Sukumar Uday Kumar**[†], **Yitian Zeng**[§], **Rayhaneh Afjei**[†], **Elise Robinson**[†], **Kenneth Lau**[‡], **Abel Bermudez**[‡], **Frezghi Habte**[†,‡], **Sharon J. Pitteri**[‡], **Robert Sinclair**[§], **Juergen K Willmann**[†], **Tarik F. Massoud**[†], **Sanjiv S. Gambhir**[†,‡,§], **Ramasamy Paulmurugan**[†,‡]

[†] Molecular Imaging Program at Stanford (MIPS) and Bio-X Program, Department of Radiology, Stanford University, Stanford, California 94305-5427, United States

[‡] Canary Center at Stanford for Cancer Early Detection, Department of Radiology, School of Medicine, Stanford University, Stanford, California 94305-5427, United States

[§] Department of Materials Science and Engineering, Stanford University, Stanford, California 94305-4034, United States

Abstract

MicroRNAs are critical regulators of cancer initiation, progression, and dissemination. Extensive evidence suggests that the inhibition of over-expressed oncogenic miRNA function can be a robust strategy for anticancer therapy. However, *in vivo* targeted delivery of miRNA therapeutics to various types of cancers remains a major challenge. Inspired by their natural synthesis and cargo delivery capabilities, researchers have exploited tumor cell-derived extracellular vesicles (TEVs) for the cancer-targeted delivery of therapeutics and theranostics. Here, we investigate a TEV-based nanoplatform for multimodal miRNA delivery and phototherapy treatments as well as the magnetic resonance imaging of cancer. We demonstrated loading of anti-miR-21 that blocks the function of endogenous oncogenic miR-21 over-expressed in cancer cells into and subsequent delivery by TEVs derived from 4T1 cells. We also produced Cy5-anti-miR-21-loaded TEVs from two other cancer cell lines (HepG2 and SKBR3) and confirmed their robust homologous and heterologous transfection efficiency and intracellular Cy5-anti-miR-21 delivery. Additionally,

Author Contributions

R.P. and R.J.C.B. designed the experiments for this study; R.J.C.B., Y.Z., S.U.K., R.A., K.L., A.B., F.H., E.R., and R.P. carried out the experiments and were involved in data acquisition and analysis. R.J.C.B., S.J.P., R.S., J.K.W., T.F.M., S.S.G., and R.P. wrote and edited the manuscript.

ASSOCIATED CONTENT Supporting Information

The Supporting Information is available free of charge on the ACS Publications website at DOI: 10.1021/acsnano.8b02587.

Figures showing schematic flow charts and overviews, TEM images, time-dependent intracellular characteristics, phase-contrast and fluorescence microscopic images, quantification of concentration-dependent fluorescence, production of HepG2-derived and SKBR3-derived TEVs, flow-cytometry-based direct quantification, transfection efficiency, cancer-cell-specific uptake, a sunburst chart, cell adhesive proteins, NTA analysis, nanoparticle tracking analysis, UV–vis spectra, TEM–EDX and STEM–EDX characterization, an SDS–PAGE profile, TEV and TEV-GIONs uptake, 4T1-cell-derivced TEVs, and the biodistribution of free ICG (PDF)

Tables showing DLS analysis and parameter details (PDF) A table showing a description of proteins identified by LC–MS (XLSX)

A video showing enhanced tropism and uptake of TEVs from 4T1 cells (AVI)

The authors declare no competing financial interest.

TEV-mediated anti-miR-21 delivery attenuated doxorubicin (DOX) resistance in breast cancer cells with a 3-fold higher cell kill efficiency than in cells treated with DOX alone. We then investigated TEVs as a biomimetic source for the functionalization of gold-iron oxide nanoparticles (GIONs) and demonstrated nanotheranostic properties of TEV-GIONs in *vitro.* TEV-GIONs demonstrated excellent T2 contrast in in *vitro* magnetic resonance (MR) imaging and resulted in efficient photothermal effect in 4T1 cells. We also evaluated the biodistribution and theranostic property of anti-miR-21 loaded TEV-GIONs *in vivo* by labeling with indocyanine green near-infrared dye. We further validated the tumor specific accumulation of TEV-GIONs using MR imaging. Our findings demonstrate that the distribution pattern of the TEV-anti-miR-21-GIONs correlated well with the tumor-targeting capability as well as the activity and efficacy obtained in response to doxorubicin combination treatments. TEVs and TEV-GIONs are promising nanotheranostics for future applications in cancer molecular imaging and therapy.

Graphical Abstract

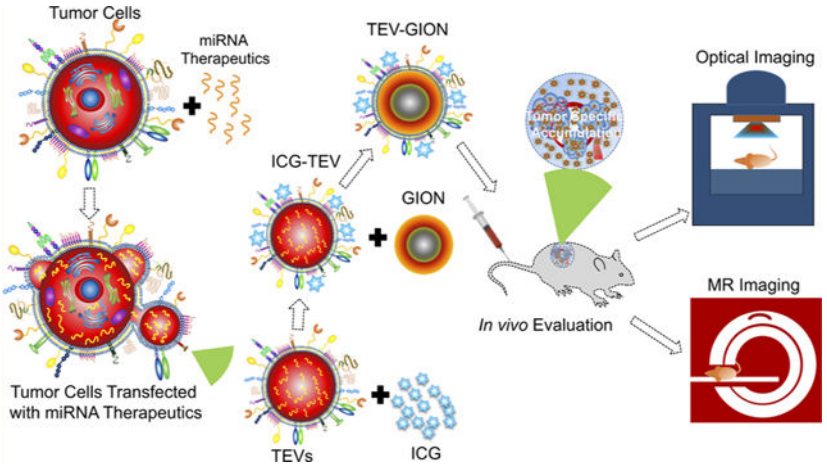

Keywords

extracellular vesicles; miRNA therapeutics; cancer nanotheranostics; breast cancer; molecular imaging; luciferase; MR imaging

MicroRNAs (miRNAs or miRs) are endogenously expressed small non-coding RNAs that regulate gene expression by controlling mRNAs at the post-transcriptional level *via* either translational repression or mRNA degradation.[1] In cancer, dysregulated miRNA expression contributes to the oncogenic, drug-resistant, and metastatic properties of neoplastic cells.[2] Numerous miRNA-targeted therapeutics have reached clinical translation, including miR-34 and antisense miRNA (anti-miR) targeting miR-122.[3,4] The ability to modulate miRNA expression and activity *in vivo* creates an opportunity for the development of innovative therapeutic approaches to cancer.[5] In general, anti-miRs offer a potentially effective tool for treatment of a variety of diseases, including cancer, cardiovascular diseases, neurological disorders, and infectious diseases. Unfortunately, synthetic naked miRNAs and anti-miRs are sensitive to nucleases in circulating plasma; therefore, effective shielding agents are required for the delivery of these nucleic acids *in vivo*.[6] Especially, clinical application of

miRNA therapies are hindered by the instability of RNA molecules in the circulation and lack of efficient vectors that can deliver RNAs to target tissues and into diseased target cells. Synthetic polymer and lipids as well as virus-based vectors are among the most widely explored vehicles for RNA delivery, but clinical progress has been limited as a result of issues related to toxicity, immunogenicity, and low efficiency. The recent discovery of extracellular vesicles (EVs) as endogenous RNA carriers allows their use to display better biocompatibility and higher delivery efficiency compared with the synthetic nano-carriers. Hence, EV-based gene therapy has already sparked general interest in both academia and industry. In this study, we investigate an efficient tumor cell-derived extracellular vesicle (TEV)-based nanoplatform for targeted delivery of anti-miR-21 in cancer therapy. We demonstrate the loading and delivery of therapeutic anti-miR-21 into cancer cells and use TEVs as a biomimetic source for the functionalization of gold–iron oxide nanoparticles (GIONs) as nanotheranostics.

TEVs (also known as microparticles, shedding vesicles, or oncosomes) are naturally synthesized nanocarriers varying in size from 100 to 1000 nm. They form by the outward budding of the plasma membrane domains, and are secreted by cells into the extracellular environment in the form of exosomes, micro-vesicles, or apoptotic bodies. Based on their capacity to deliver functional biomolecules *(e.g.,* short interfering RNAs, miRNAs, mRNAs, and proteins) between cells, and their high versatility for customization, the therapeutic use of na $\ddot{i}$ ve or customized TEVs has been investigated recently.[7,8] MiRNA-21 is a potent oncomiR over-expressed in most cancers.[8] Recent studies have demonstrated the use of antisense miRNA-21-based molecular therapy in breast cancer,[9] hepatocellular carcinoma,[10] and brain cancer.[11] Over-expression of oncomiR-21 has been observed in most of cancers. MiRNA-21 has been implicated in a number of cellular processes, including chemotherapy resistance, possibly by directly modulating the expression of several apoptotic related proteins including Bcl-2 protein expression. In addition, it was well-demonstrated that the role of miR-21 in cancer chemo resistance and miR-21 silencing significantly increased the chemotherapy sensitivity of various drugs and decreased the expression of multidrug resistance genes.[12]

Theranostic nanostructures that combine both diagnostic and therapeutic components within a single nanoscale platform have attracted major interest in recent times[13] because they would enable both highly specific detection and a subsequent targeted image-guided treatment approaches, potentially within a single clinical procedure.[14] Oligonucleotides, such as small interfering RNA and microRNA, which are powerful therapeutic agents, have been effectively employed in theranostic systems against various cancers. The use of quantum dots, iron oxide nanoparticles, and gold nanoparticles has facilitated early detection of tumors and evaluation of therapeutic efficacy. Among these nanotheranostics, GIONs have been of great interest in multimodal cancer imaging owing to the complementary features of superparamagnetic iron oxide nanoparticles (SPIONs) and gold nanoparticles.[15] SPIONs are attractive magnetic resonance imagine (MRI) contrast agents on account of their super-paramagnetic behavior, and gold can be used as a computerized tomography (CT) contrast agent.[16] As such, GIONs can provide a synergistic effect in multimodal imaging techniques including CT, MRI, photoacoustic imaging, and surface enhanced Raman

spectroscopy.[16] Additionally, GIONs can be used as hyperthermia agents to selectively damage cancerous cells through thermal ablation.[17] Of note is the fact that the coating and surface functionalization of GIONs is essential to providing tumor targeting, enhancing their stability, and concealing them from a host immune system.[18] Driven by the concept of bridging synthetic and natural biomaterials for nanoparticle functionalization[19,20] and by our recent success in transferring intact membranes and engineered CXCR4 proteins from human adipose-derived stem cells to the exterior of soft colloidal nanoparticles made of poly(lactic-co-glycolic) acid, here, we construct TEVs that camouflage nanotheranostic TEV–GIONs. This could serve as a multifunctional nanoplatform for simultaneous cancer imaging and therapy (miRNA and photothermal ablation) while improving tumor-specific targeting without perturbing the immune system. Several other groups have previously coated metallic particles with cell membranes, including erythrocytes. However, the isolation and processing of plasma membranes is more laborious than our current strategy. The approach reported here, with its simplicity in preparation of cell derived materials and simple loading of miRNAs in TEVs and GION functionalization, offers an innovative theranostic platform for cancer therapy and imaging. Additionally, TEV-mediated anti-miR-21 delivery shows an excellent additive effect with doxorubicin (DOX), also attenuating DOX resistance in breast cancer cells and yielding a 3-fold higher cell kill efficiency than in cells treated with DOX alone. Moreover, TEV–GIONs provide an excellent multimodal contrast agent for T2-weighted MR imaging and combined chemo-sensitizing miRNA and photothermal effects of TEV–GIONs *in vitro.* Herein, we also show the *in vivo* biodistribution of TEV–GIONs using indocyanine green (ICG) dye-mediated near-infrared (NIR) imaging and T2-weighted magnetic resonance (MR) imaging, the anti-miR-21 levels by qRT-PCR, and anti-miR-21 and DOX combination therapy in 4T1 syngeneic tumor by bioluminescence imaging.

RESULTS AND DISCUSSION

Preparation of Tumor Cell-Derived Extracellular Vesicles Packed with Chemosensitizing miRNA Therapeutics.

We aimed to demonstrate two functional applications of TEVs: (1) as an efficient nanocarrier platform for the cancer-cell-specific delivery of chemo sensitizing anti-miR-21 and (2) as a cancer-cell-mimicking functionalization source for gold–iron oxide nanotheranostics. First, we prepared the (Cy5-anti-miR-21)-loaded TEVs as a nanocarrier platform for therapeutic delivery of miRNA, as shown in Scheme 1. Figure S1 outlines the experimental steps we used to load theranostic Cy5-anti-miR-21 and GIONs for monitoring TEVs delivery and function in cancer cells. To date, various strategies have been employed to load cargo miRNAs into TEVs,[21] which include exogenous loading by electroporation, in which oligonucleotides were directly introduced into TEVs, and endogenous loading by engineering cells to over-express target miRNAs, where the TEVs-producing cells were transfected with plasmid vectors expressing target miRNAs.[21,22] Here, we demonstrate a differential loading model in which synthetic anti-miR-21 is directly transfected to TEVs-producing donor cells. This strategy was robust and showed a very high level of loading (Figure 1) that cannot be achieved by the above-mentioned previous two methods.

Cell-Derived Vesicles as a New Class of Bioinspired Therapeutics and Theranostic Delivery Systems.

Compared with the synthetic liposomes and other conventional nanocarriers, cell-derived vesicles (CDV) have exceptional advantages such as biocompatibility, minimal toxicity, non-hazardous qualities, ease of engineering and packaging of a diverse group of agents, provision of enhanced tissue-specific delivery, ability to be produced on a large scale with a reduced cost. Cell-based therapies use viable cells for the treatment of various diseases. In particular, chimeric antigen receptor (CAR) T-cell therapy, together with checkpoint inhibitors, have been celebrated as a breakthrough technology due to the substantial benefit observed in clinical trials with patients suffering from relapsed or refractory B-cell malignancies. Therapeutic cell manufacturing, clinical efficacy, and related toxicities are the major challenges that need to be resolved. Cell-free synthetic biology emerges as a powerful and flexible enabling technology that can engineer biological parts and systems for life science applications without using living cells. This technology provides simpler and faster engineering solutions with an extraordinary freedom of design in an open environment as compared with cell systems, and thereby, we can enhance the therapeutic efficacy with or without minimal toxicities. We envisioned the cell vesicles with functional enhancement by means of genetic engineering, to mitigate the challenges associated with cell-based therapies. In addition, presently cell therapy requires the *ex vivo* manipulation of patient-derived autologous cells or gene engineering. In the future, cell free therapeutics could be used by the in *situ* engineering of cells obtained from patients.

Cancer Cell Specific Uptake and Intracellular Release of Cy5-anti-miRNA-21.

It has been previously shown that TEV internalization is an active and energy-dependent endocytic process.[23] To investigate cellular uptake and release of intracellular Cy5-anti-miRNA-21, we initially examined the time- and concentration-dependent homologous tumor cell uptake of donor 4T1 TEVs-Cy5-anti-miRNA-21 in recipient 4T1 cells (Figures S3 and S4). Shortly after incubation with TEVs, we observed a punctuated pattern of intracellular fluorescence, with increasing signal over time. As expected, the Cy5-fluorescence signal intensity increased with the time of incubation and concentration of TEVs. For instance, the total cell fluorescence intensity of 4T1 cells treated with 15 μg/mL of TEVs showed significantly ($p < 0.01$) higher Cy5 fluorescence intensity than the control cells or cells treated with 5 μg/mL of TEVs, demonstrating that the transfection efficiency of the TEVs was significantly dependent on their concentration. To confirm this, we performed qualitative real-time polymerase chain reactions (qRT-PCR) to quantify the delivered anti-miR-21 levels from the recipient 4T1 cells treated with different concentrations of anti-miR-21 TEVs.

As shown in Figure 1i, the 4T1 cells treated with TEVs-Cy5- anti-miR-21 (5,10,15, 20,25, and 30 μg/mL) showed anti-miR-21 dose-dependent reduction in endogenous miR-21 levels for up to 25 μg/mL of TEVs but showed significant fluctuation after 30 μg/mL of TEVs. We observed this result consistently in several repeated experiments, and this maybe owing to cell death induced by the high dose of TEV-anti-miR-21 treatment. In contrast, TEVs-Cy5-anti-miR-21 treated recipient 4T1 cells showed concentration-dependent increase in anti-miR-21 expression levels (Figure 1j). Additionally, our experimental results shows that the

higher concentration of TEV-AmiRNA-21 (25 μg/mL) treatment shows the functional saturation in endogenous miRNA-21 expression interference. However, cells transfected with EVs of more than 25 μg/mL the delivered AmiRNA-21 levels are 600 000-fold higher than the untreated cells. This is likely owing to the cells transfected with EVs of more than 20 μg/mL generating significant levels of cell death and shows differential response due to the extraction of some sticky EVs tagging along with the dead cells while extracting RNAs. As shown in Figure 1i, the 4T1 cells treated with TEVs-Cy5-anti-miR-21 (5, 10, 15, 20, 25, and 30 μg/mL) showed lower endogenous levels of miR-21 compared with cells treated with control TEVs or without any treatment for up to 25 μg/mL of TEVs-Cy5-anti-miR-21 treatment. In contrast, TEVs-Cy5-anti-miR-21-treated recipient 4T1 cells showed concentration-dependent increases in anti-miR-21 levels (Figure 1j). We also tested the functionality of the delivered anti-miR-21 by measuring the miR-21 downstream expression of target genes. We observed a significant level of increase in PTEN and PDCD4 apoptotic protein levels, with a concomitant increase in apoptotic Bcl2 levels (Figure 1k). Next, we evaluated the generalizability of this TEVs-based nanoplatform by studying heterologous tumor cell uptake and release of TEVs-Cy5-anti-miR-21. To that end, we produced Cy5-anti-miR-21 loaded TEVs from human hepatocellular carcinoma cells (HepG2) and breast cancer cells (SKBR3). Figures S5 and S6 showthe production of HepG2 and SKBR3 donor cell-derived TEVs-Cy5-anti-miR-21. Flow cytometry (Figure S7) confirmed the presence and comparative packing efficiency of Cy5-anti-miR-21 within TEVs released from different donor cells (4T1, HepG2, and SKBR3). We then investigated the cross-transfection and intracellular delivery of TEVs-Cy5-anti-miR-21 derived from homologous (4T1) and heterologous cancer cells (HepG2 and SKBR3). Fluorescence micrographs (Figures S8–S10) and flow-cytometry results (Figure S11) revealed the transfection efficiency of TEVs in homologous and heterologous cells. The transfection of HepG2 cells using donor breast cancer (4T1 and SKBR3) cell-derived TEVs, and transfection of breast cancer cells using HepG2 donor cell-derived TEVs showed the robust uptake and intracellular release of Cy5-anti-miR-21. We also examined the uptake efficiency of TEVs, and whether this was dependent on the malignant state of the cell. We therefore tested this in both neoplastic (4T1) and non-neoplastic (mouse fibroblast, HEK-293T) cells. Figure 12 shows that the 4T1 cancer cells treated with 4T1-derived TEVs-Cy5-anti-miR-21 (1.5×10^{11} TEVs/mL) showed significantly higher uptake compared with HEK293T and mouse fibroblast cell lines.

We also examined active mobility, uptake, and intracellular release by 4T1-derived TEVs in multiple cancer cells. For this purpose, we first immobilized the 4T1-TEVs in matrigel and then different human cells (ovarian, Hey cells; glioblastoma, U87MG, Ln308, and Ln229; hepatocellular carcinoma, HepG2; and immortalized control cells, HEK293T) were plated on top of the immobilized TEVs. Figure 2a shows the scheme of the experimental setup, and Figure 2b–i and Video S1 show the enhanced tropism and uptake of TEVs from 4T1 cells by other cancer cells (HepG2, U87MG, Ln308, Hey, and Ln229). Interestingly, the co-incubation of TEVs with HEK293T (non-neoplastic in origin) showed minimal fluorescence signal, likely owing to the lower adhesion and uptake of TEVs.

Proteomic Profiling of TEVs.

It has been well-demonstrated that the number of cancer cell surface proteins (the CCAMs) mediate both homophilic and heterophilic adhesion between cancer cells of different types.[24] Most CCAMs are uniformly distributed along the plasma membrane of cancer cells that contact other cells, and the cytosol-facing domains of these proteins are usually connected to elements of the cytoskeleton. Because TEVs are formed by the outward budding of the plasma membrane (PM) domains, we speculate that TEVs may have CCAMs and other biomolecules that possibly enhance the tumor cell specific adhesion and uptake of TEVs. For this purpose, we performed the proteomic analysis of TEVs using Liquid Chromatography—Mass Spectrometry (LC–MS). Figure S13 shows the schematic view of qualitative proteomic analysis, evaluating the presence of proteins identified by at least a minimum of three distinct peptides. A total of 612 proteins were identified, of which 360 were membrane proteins of TEV specific and another 252 were from small exo-like EVs (sEXo-EVs) (Figure S14). The majority of proteins were common to TEVs and sEXo-EVs fractions, but each fraction contained a restricted set of unique proteins as well. Tables S2 and S3 show the major proteins identified in TEVs and sEXo-EVs fractions (we omitted probable contaminants and minor proteins in our analyzed results). To determine the subcellular origin of the TEVs membrane proteins, we investigated the subcellular location of identified TEVs proteins. According to the sources (Gene Ontology, GO) we used to annotate membrane association and subcellular location; 49% could be annotated to the plasma membrane, 38% were from the cytosol compartments, 21% came from the cytoskeletal organization, and another 18% could be annotated as secreted vesicles (Figures S14 and S15). We classified TEV proteins further based on membrane protein functions. Among the identified membrane proteins of TEVs and sEXo-EVs, fibronectin, amino acid and ion transporters (Na^+/ K^+-ATPase), CCAMs, stress responsive proteins (heat-shock proteins) and other proteins related to cell growth and differentiation were highly represented. Moreover, functional classification of plasma membrane proteins identified from the TEVs fractions (Figures S16 and S17) clearly showed that transporters and CCAMs were abundantly present. In particular, CCAMs, including cadherins (CDH1), catenins (CTNA1 and CTNB1), integrins, immunoglobulin superfamily cell adhesion molecules (CD166), and tetraspanins (CD9 and CD151), were predominantly found in the TEVs and sExo-EVs fraction. Additionally, epithelial cell adhesion molecule (EPCAM) and cell surface glycoprotein MUC18 (MCAM) were highly represented in our MS data. We observed that G proteins and the cortical cytoskeleton were also highly represented in the TEVs and sExo-EVs fractions. For instance, the three ERM proteins (ezrin, radixin, and moesin) that are known to be commonly up-regulated in a variety of aggressive cancers and are actively involved in cell signaling and cytoskeletal dynamics at the plasma membrane[25] were strongly expressed in TEVs. A number of other structural proteins that are affiliated with the cortical cytoskeleton were found in our MS data, and many were differentially expressed in the TEVs. Intermediate filaments such as tubulins, actins, and myosins were also present in the isolated TEVs. In summary, having examined the proteome of TEVs, we identified a number of proteins that may contribute to the molecular mechanisms involved in cancer cell specific adhesion and contributing to the strong uptake of TEVs. We identified several adhesion proteins that potentially participate in homologous and heterologous cancer cell adhesion.[20] Our findings provide the foundation for future studies that will focus on cell

adhesive properties ofTEVs, and that could be exploited for the development of future TEVs-based therapies for cancer. The strong uptake of TEVs by source cells indicates that specific adhesive protein-mediated processes likely facilitate this transport.[26]

Chemosensitizing Effects of TEV-anti-miRNA-21 on 4T1 Cells.

To further assess the therapeutic potential of TEV-anti-miRNA-21, we also hypothesized that by administering a low dose of a cytotoxic chemotherapeutic *(e.g.,* doxorubicin), we could amplify the effectiveness of TEV-anti-miRNA-21. Mainly, we posited that low-dose doxorubicin would serve to inhibit the cell cycle and slow down the rate of cell division, as shown by us previously.[9] We observed that upon the combination treatment with TEVs-anti-miRNA-21 (0.5 mmol/L) and low-dose doxorubicin (IC_{50}: 1 μMmol/L), the 4T1 tumor cells acquired a spindle-like shape, detached from the plate, and died through apoptosis (Figure 3). This corresponded to a significant induction of apoptosis and decrease in proliferation. Importantly, increased apoptosis was not seen in the absence of TEV-anti-miR-21 nor was it seen in cells treated with doxorubicin alone. To quantify the chemosensitizing effects of TEV-anti-miRNA-21 on 4T1 cells, we assessed apoptotic rates by propidium iodide (PI)-staining-based FACS analysis. The percentages of apoptosis in cells cotreated with control EV and doxorubicin were not significantly different from untreated control cells for up to 0.5 μM of DOX, but in cells co-treated with TEV-anti-miRNA-21 and DOX, it was nearly 15.3% (0.25 μM DOX) and 16.7% (0.5 μM DOX) (Figure 3a). Similarly, the no-treatment control group and TEV-anti-miR-21 alone treatment group showed no significant increase in apoptotic cells. At 1 μM DOX treatment the cells co-treated with control EV showed only 10% of cells in the apoptotic window, while the same was nearly 40% in cells cotreated with TEV-anti-miRNA-21 (Figure 3a). These results clearly support the role anti-miR-21-mediated enhancement of PTEN and PDCD4 expression (Figure 1k) and the associated enhancement of cell response to chemotherapy. A similar effect was also observed in cell cycle analysis of the samples (Figure 3b).

Preparation and Characterization of TEVs-Coated Gold–Iron Oxide Nanoparticles.

The fabrication strategy for the TEV-GIONs is shown in Scheme 1 and consisted of the isolation and purification ofTEVs-Cy5-anti-miR-21 from donor 4T1 cells, and fusion of the TEVs membrane vesicles with the multifunctional GIONs. This hybrid multifunctional system was constructed by wrapping TEVs membranes onto the GIONs. The iron oxide acts as a strong T2 contrast agent for MRI, and the gold coated on the iron oxide core can act as a photosensitizer by converting deeply penetrating NIR light to heat (wide absorption spectrum of gold). The Cy5-anti-miR-21 packed TEVs provide the biomimetic surface to help avoid immune clearance, prolong blood circulation time, and improve tumor targeting and subsequent miRNA-mediated therapeutic efficacy as well as delivery of the GION cores to enhance possible photothermal ablation. Briefly, the preformulated GIONs were fused with TEVs via a modified top-down process.[18] The GIONs (Z average size of 70 nm) and the TEVs (Z average size of 160 nm) were extruded through 100 nm porous membranes and generated TEVs-GIONs with a hydrodynamic diameter (Z average size) of 97 nm. These samples were analyzed by nanoparticle tracking analysis (NTA). Figures 4a–c and S18 and Table S1 show the comparative results measured by dynamic light scattering (DLS) and NTA. The TEVs and GIONs mixture ratio was optimized with the surface area calculation as

discussed previously,[18] and Tables S1 and S2 show the parameters that were considered for optimization. The TEVs and GIONs were repeatedly passed through the extruder to ensure that they were completely coated with a homogeneous lipid shell (Figure S19). To further confirm the presence of the hybrid metallic core of GIONs, an external magnet was used to separate TEV-GIONs from the uncoated TEVs (Figure S20), and the separated GIONs and TEV-GIONs were then suspended in deionized water and analyzed by UV–vis spectroscopy (Infinite M1000, Tecan-Safire) by scanning from 400 to 700 nm. Optical measurements of TEVs functionalized GIONs confirmed NPs identity and functionalization (Figure S21). Colloidal gold nanoparticles exhibit UV–vis maximum absorbance values ranging between 510 and 550 nm, in agreement with the GIONs and TEV-GIONs showing the peaks at approximately 520 nm, which primarily confirm the presence of the GION cores. In comparison, previously synthesized PEGylated citrate gold nanoparticles displayed a maximum wavelength of 533 nm.[27]

Transmission Electron Microscopy and Energy-Dispersive X-Ray Spectra Analysis.

We performed TEM and Scanning Transmission Electron Microscopy—Energy-Dispersive X-ray (STEM—EDX) analysis to further confirm the core—shell structure of TEVs-GIONs and to validate the hybrid metallic nature of GIONs core. *Via* electron microscopy, we observed the GIONs core and TEVs shell of TEVs-GIONs (Figure 4c—e). Gold in GIONs as well as TEV-GIONs shows higher contrast for TEM imaging because Au has a much larger electron density than biomolecules. Furthermore, the GIONs core displayed a strongly intense and distinctive Au peak at 9.7 keV, and a separate strong uranium peak was seen from the lipid layer shell owing to the negative staining of TEVs lipid vesicles. Moreover, STEM—EDX analysis revealed the existence of the bimetallic hybrid core, wrapped in a lipid layer (shell) (Figures S22 and S23). The surface ζ potential also suggested successful TEVs coating. The surface charge ofcitrate-coated GIONs had a negative peak at —17 mV, which further reduced down to —29 mV upon coating GIONs with TEVs (Figure 4c and Table S1). This negative ζ potential was likely owing to the presence of charged molecules, such as glycolipids and glycoproteins, on the 4T1-derived TEVs-coated GIONs.[28] Based on previous studies of cell membrane-coated particles, the TEV membrane coating on the GIONs should transfer the membrane bilayer structure onto the nanoparticle surface, which is important to allow the GIONs to mimic the cancer cell homologous and heterologous adhesion capabilities during their interactions with the cancers. To verify the successful functionalization of obtained GIONs with TEVs membrane, the protein contents of the particles were examined using sodium dodecyl sulfate—polyacrylamide gel electrophoresis (SDS-PAGE; Figure S24). The SDS-PAGE protein profiles of the TEVs and the TEVs-GIONs matched relatively closely, indicating that the present approach leaves membrane proteins embedded in the same physiological membrane and confirmed the successful relocation of TEVs proteins onto the surface of the GIONs.

Intracellular Delivery of Nanotheranostics.

To confirm the coexistence of anti-miR-21 and TEVs on the GIONs *in vitro,* the cell membrane vesicles were labeled with green fluorescent dye (DiO), and anti-miRNA-21 was labeled with the red fluorescent Cy5 dye, prior to the particle—vesicle fusion. These dual-fluorophore-labeled TEVs-GIONs were incubated with 4T1 cells followed by fluorescence

microscopy. As shown in Figure 4f,there was an overlap of DiO (green) and Cy5 (red) light fluorescence, demonstrating the complete core—shell structure of the TEVs-GIONs after internalization by cells, which would be of benefit to the intracellular delivery of nanotheranostics. In addition, to test the specificity of TEV and TEV-GIONs uptake, we transfected an equal number of TEVs and TEV-GIONs into RAW264.7 macrophages cells and measured the uptake by fluorescent microscopy of Cy5 fluorescence arising from Cy5-anti-miR-21. The cells treated with cationic liposomes labeled with DiD dye were used as the positive control. The result showed significant levels ofuptake of cationic liposomes by the cells; in contrast, we did not observe significant Cy5 signal from cells treated with TEVs and TEV-GIONs (Figure S25). This result clearly confirms that the cancer cell uptake of TEV is specific.

Evaluation of Absolute Number of Anti-miR-21 Transferred at Each Stage of Its Use in TEV and TEV-GIONs Transfection in Cells.

The delivery of anti-miR-21 by TEVs is one of the important objectives of this study, and thus to provide clear illustration on the fate of anti-miR-21 at different stages of its production, processing, and characterization in the workflow outlined herein, we quantified anti-miR-21 at each stage, starting from anti-miR-21 transfection in 4T1 cells, until the last stage, in which TEVs and TEV-GIONs were used for transfection. We used Taqman qRT-PCRfor evaluation. The results of this study clearly establish quantitative validation of anti-miR-21 loaded TEV synthesis as well as its transfection efficacy in terms of anti-miR-21 copy number (Figure 5). Absolute quantitation of anti- miR-21 was achieved using a standard curve, constructed by amplifying known amounts of anti-miR-21 in a parallel group of reactions run under identical conditions to that of the sample. The result showed that when using lipofectamine, ~77% of 5 nmols used for transfection were able to enter inside the cells whenweused4 × 10^6 cells for transfection (Figure 5d).Wefound ~90–120 copies of anti-miR-21 per EV independent of their extrusion process (in both TEVs and TEV-GIONs). The TEVs before and after GION loading showed no significant change in the number of anti-miR-21 per EV. The transfection of 4T1 cells with TEV and TEV-GION (6 × 10^9 TEV/ml) showed ~20% of anti-miR-21 delivered into the recipient cells (Figure 5). The results clearly confirm that the extrusion of GIONs in TEVs is not interfering with the transfection efficiency of TEVs in recipient cells or the anti-miR-21 loading in TEVs. Interestingly, the presence of GIONs in TEVs (TEV-GIONs) showed slight improvement in transfection efficiency in recipient cells compared with TEVs (~15% more than TEVs).

MR Imaging in Cells Treated with TEVs and TEV-GIONs.

To examine the feasibility of using TEVs-GIONs as multimodal contrast agents, we performed T2-weighted MRI of 4T1 cells incubated with GIONs, TEVs, and TEV-GIONs, respectively (Figure 6a). As expected, GIONs and TEVs-GIONs showed T2 hypointensity because high T2 relaxivity enables SPIONs to generate strong negative T2 contrast in MR imaging. Additionally, the low T2 signal was only produced by iron oxide-containing samples (GIONs, TEV-GIONs, and TEV-Cy5-anti-miR-21), clearly indicating the presence of embedded SPIONs in the inner core of GIONs. These *in vitro* imaging results demonstrated that TEVs-GIONs could be additionally used as MRI contrast agents.

Photothermal Therapy.

The impact of photothermal therapy (PTT) in treating cancer has been on the increase owing to the enhanced photothermal capabilities by offering next generation nanoscale photothermal agents. Among these nanoscale agents, gold NPs are also recognized by their PTT capabilities, converting electromagnetic radiation into heat due to electron excitation and relaxation, which has been used for thermal ablation of tumor cells.[29,30] Since it has been demonstrated that normal cells are less susceptible to heat compared with cancerous cells,[31] PTT has been considered as a potentially safe treatment strategy for cancer. We thus incubated GIONs, TEVs, and TEVs-GIONs with 4T1 cells for 24 h and then removed the free nanoparticles in each well by repeated washing with phosphate-buffered saline (PBS). We then exposed the 4T1 cells to a 980 nm laser for 15 min. After hyperthermia treatment, the cells were further cultured for 24 h under standard conditions for recovery. To assess for 4T1 cell viability, we added 2 μM of propidium iodide to each well and incubated the solution at 37 °C for 15 min. Fluorescence was evaluated using an Olympus microscope equipped with a digital camera after washing the cells once with PBS. Cells not exposed to irradiation were considered as controls. We found that the TEVs-anti-miRNA-21 functionalization on GIONs resulted in higher cytotoxicity, while untreated cells retained their viability. Moreover, the observed cytotoxicity of TEVs-GIONs was higher than that seen in the TEVs-anti-miRNA-21 or TEVs treatment groups (Figure 6b). These observations confirm the photo thermal effects of TEVs-GIONs. The same experiment quantitatively evaluated for cell viability 48 h after photothermal therapy by cell titer blue assay showed significantly ($p < 0.001$) reduced cell viability in cells treated with TEV-anti-miR-21, TEV-anti-miR-21-GION, and TEV-anti-miR-21-GION plus photothermal therapy compared with control and control—TEV treatment (Figure 6c). TEV-anti-miR-21-GION with photothermal therapy showed significant reduction ($p < 0.05$) in cell viability compared with cells treated with TEV-anti-miR- 21 and TEV-anti-miR-21-GION.

In Vivo Biodistribution and Antitumor Properties of TEV-GIONs and TEV-GION-anti-miR-21 in Combination with DOX Therapy.

To test the *in vivo* biodistribution and evaluate the antitumor potential of TEV-GION-anti-miR-21, we used a syngeneic subcutaneous 4T1 tumor-bearing mouse model (Figure 7a). To visualize the biodistribution of TEV-GIONs, we used the sensitive and intrinsic NIR fluorescence of ICG by conjugating NH_2 reactive ICG with TEVs. We first optimized the labeling protocol for optimal conjugation of ICG to intact TEVs. In addition, we also labeled Alexa-633 dye using the similar protocol for measuring the conjugation of TEVs using FACs analysis. After labeling, we resolved the TEV proteins in SDS-PAGE and measured for NIR fluorescence using an *in vivo* imaging system (Figure 7b, left). We also observed the ICG-labeled TEVs under a fluorescence microscope using a Cy7 filter, and the results showed efficient labeling of intact TEVs (Figure S26). Similarly, the FACS analysis of Alexa-633 labeled TEVs showed a significant fluorescence shift compared with unlabeled TEVs (Figure 7b, right).

We used the ICG-labeled TEV-GION or TEV-GION-anti-miRNA-21 NPs for biodistribution and therapeutic studies in animals. We used control animals injected with similar concentrations of ICG, based on ICG quantification using spectroscopy to observe the free

ICG biodistribution pattern (Figure S27). The animals bearing 4T1 subcutaneous syngeneic tumors were used for TEV biodistribution and tumor specific accumulation. We measured the amounts of the TEV-GION-ICG or TEV-GION-anti-miRNA-21-ICG NPs accumulated in tumor and other organs using the sensitive NIR fluorescence imaging of ICG. Figure S27 shows that the fluorescence signals of free ICG at 1 h after injection were distributed in the entire body with predominant accumulation in the liver, spleen and lungs. In contrast, after 24 h, the free ICG distribution was uniform throughout the body. The *ex vivo* analysis shows that fluorescence signals of the free ICG group at 24 h were mostly in the liver and were almost cleared from other organs, where no obvious signals were detected (Figure S27; note that the scale bar is adjusted for viewing the low amount of signal). However, the TEV-GION-ICG or TEV-GION-anti-miRNA-21-ICG showed a different biodistribution pattern. The ICG fluorescence intensity throughout each nude mouse, even after 12 days of repeated injection for TEV-GION-ICG or TEV-GION-anti- miRNA-21-ICG, was still strong, with high accumulation in the tumor (Figure 7). These data further confirmed that incorporation of ICG with TEVs could significantly reduce the clearance from the body and the degradation of free ICG. In the meantime, the TEV-GION-ICG or TEV-GION-anti-miRNA-21-ICG NPs located in the liver and around the tumor at 24 h, and fluorescence signals in the tumor at 24, 48, and 72 h, were progressively stronger (Figure 7c,d), indicating the accumulation of nanoparticles at the tumor sites. As the observation periods were extended for the second and third doses, both NPs that continuously accumulated at the tumor site exhibited apparent fluorescence signal at the tumor sites (circled around the tumor), indicating a distinctive targeting ability of TEV-GIONs. Relatively strong fluorescence could be observed after 4 days, while fluorescence signals from other parts of the body appeared to diffuse toward the tumor, signifying the targeted migration of TEV coated NPs.

This observation was further validated by T2-weighted MR imaging. On day 12, both NP-treated groups, along with control mice, were imaged using a 3T MR scanner. The T2-weighted gradient echo imaging (Figure 7ciii,diii) showed significant accumulation of TEV-GION NPs in the tumors, as evidenced by the increased susceptibility effect, as well as T2 hypointensity in the areas of the tumor mass. The region of interest analysis of MRI signal change showed a strong T2 signal reduction in animals receiving TEV-GION NPs in comparison with control mice (Figures 7c,d and S27).

After observing the whole-body biodistribution of TEV- GION-ICG in different organs, we next evaluated the distribution of delivered anti-miRNA-21 in tumors and major organs using an ultrasensitive quantitative RT-PCR method. For anti-miR-21 quantification, the mice were sacrificed after the twelfth day, and the tumor and major organs were collected and used for total RNA extraction. As expected, a significant amount of GION-anti-miRNA-21 was delivered into 4T1 tumors as compared with other organs suggesting the potential use of TEV-mediated delivery of miRNA/nucleic acids for cancer therapies (Figure 7g). We also found significant accumulation of anti-miRNA-21 in the liver, lung, and brain. We speculate that this is likely owing to the surface adhesive proteins, in particular the integrins of TEVs, possibly playing a role in this organ specific accumulation. Consistent with earlier reports and our proteomic analysis, integrin expression profiles correlated with organ tropism of TEV-GION-anti-miRNA-21 (Figure 27).[32]

We also evaluated the antitumor effect of TEV-GION or TEV-GION-anti-miRNA-21 in combination with DOX in animals bearing syngeneic 4T1 tumors. The response to treatment were investigated in living mice by optical bioluminescence imaging. Syngeneic subcutaneous tumor xenografts of 4T1-Fluc-eGFP cells were established on both sides of the lower flanks of nude mice. One group of animals ($n = 3$) was treated with TEV-GION and DOX, and the second group ($n = 3$) was treated with TEV-GION-anti-miRNA-21 and DOX. Animals were imaged by optical CCD camera for bioluminescence signal and tumor volumes were measured using digital Vernier caliper. The results demonstrate that growth of tumors established by cells treated with the TEV-GION-anti-miRNA-21 and DOX combination was significantly lower compared to the tumor growth of animals treated with TEV-GION and DOX (Figure 7e,f). Assisted by TEVs, intracellular delivery of the anti-miR-21 notably inhibits the tumor growth *in vivo* and increased the therapeutic efficacy of DOX as seen in cells.

Multidrug resistance and disease relapse is a challenging clinical problem in the treatment of breast cancer. The functional significance of miR-21 has been elucidated in several recent studies. miR-21 is now one of the most-studied miRNAs owing to its involvement in cancer progression. It has been recently indicated that miR-21 plays a critical role in regulating antiapoptosis and chemotherapy resistance in breast tumor cells.[33] In the present study, the results suggest that the TEV mediated delivery of anti-miRNA-21 obviously promoted the accumulation of anti-miR-21 in tumor, leading to the inhibition of miR-21 expression and thereby enhancing the up-regulation of apoptosis and reducing the chemotherapy resistance in breast tumors.

Additionally, we used a NIR dye-ICG incorporated TEV-GION to image the whole body biodistribution and tumor localization of NPs after intravenous (iv) injection into live mice bearing syngeneic 4T1 subcuteneous tumors. We also quantified the delivered anti-miRNA-21 distribution in tumor and major organs using an ultrasensitive quantitative RT-PCR method after i.v. injection of TEV-GION-anti-miRNA-21-ICG. We further validated the tumor specific localization of TEV-GIONs with MR imaging. We also studied the combination therapy of TEV- GION-anti-miRNA-21 plus DOX, which showed notable tumor growth reduction compared to the TEV-GION plus DOX group as measured by bioluminescence imaging. Our findings demonstrate that the distribution pattern of the TEV-GION-anti-miRNA-21-ICG correlated well with the tumor targeting capability, as well as the activity and efficacy obtained with DOX combination treatments. Together, our work not only proposes a strategy to construct a biomimetic nanotheranostic platform but also provides an alternate solution for targeted delivery of GION and antisense miRNAs.

CONCLUSIONS

In this developmental study, we developed TEVs as nanocarriers for the combinatorial delivery of therapeutic miRNA and a theranostic hybrid nanoprobe (GIONs). We demonstrated direct loading of anti-miR-21 into and subsequent delivery by TEVs derived from 4T1 cancer cells. We also demonstrated the generalizability of our method by producing Cy5-anti-miR-21-loaded TEVs from two other cancer cell lines (HepG2 and SKBR3) and confirmed robust homologous and heterologous transfection efficiency and

intracellular Cy5-anti-miR-21 delivery. Moreover, there was an excellent chemosensitizing effect of anti-miR-21 demonstrated by a greater tumor cell killing efficiency in 4T1 cells. Additionally, we report a type of cell mimicking approach using tumor cell-derived extracellular vesicles as a source for cancer cell mimicking functionalization of the GIONs. This approach simplifies and expands the arsenal of preparation methods for cell mimetic GIONs. The resulting TEV-GIONs have core–shell hybrid nanostructures determined by TEM and EDX. We further demonstrated that TEV-GIONs might potentially be used as targeted nanotheranostics for simultaneous imaging and photothermal therapy. Furthermore, we also demonstrated the *in vivo* biodistribution and tumor-specific accumulation of TEV-GION-NPs after intravenous injection into live mice bearing syngeneic 4T1-subcuteneous tumors. In addition, we demonstrated that TEV-mediated accumulation of anti-miRNA-21 in tumors and major organs using an ultrasensitive quantitative RT-PCR method. We also validated the tumor specific localization of TEV-GIONs using MR imaging. The therapeutic study also showed significant enhancement in tumor growth reduction in animals receiving TEV-GION-anti-miR-21-NPs plus DOX compared to TEV-GION-NPs plus DOX. Taken together, we show that TEVs may act as useful nanocarriers for the targeted delivery of RNAi therapeutics to cancer, and they can be used as a source for the biofunctionalization of diverse synthetic materials. CDVs represent a new generation of therapeutic delivery systems, providing high delivery efficiency, intrinsic targeting properties, and low immunogenicity. In recent years, considerable research efforts have been directed toward developing safe and efficient EV-based delivery vehicles. Even though EVs have shown great promise in therapeutic delivery, substantial improvements in exploring standardized isolation techniques with high efficiency and robust yield, scalable production, standard procedures for EV storage, efficient loading methods without damaging EV integrity, and understanding their *in vivo* trafficking in humans are considered the major hurdles necessary to be solved before clinical translation.

EXPERIMENTAL SECTION

Materials and Methods.

Materials.—Gold-coated magnetic nanoparticles were purchased from Creative Diagnostics. All other chemicals were purchased from Sigma-Aldrich and used as received. Cell-culture plates, FBS, penicillin, streptomycin, sodium bicarbonate, cell-culture medium and PBS were purchased from GIBCO BRL (Frederick, MD). Lipofectamine 2000 transfection reagent and the Vibrant Multicolor Cell-Labeling Kit containing DiOC18 (3) (3,3′-dioctadecyloxacarbo-cyanine perchlorate) (DiO), 1,1′-dioctadecyl-3,3,3′,3′-tetramethylin-dodicarbocyanine, and 4-chlorobenzenesulfonate salt (DiD) solutions, protein gels, and buffers for gel electrophoresis and immunoblot analysis were purchased from Invitrogen (Carlsbad, CA). 4′,6-Diamidino-2-phenylindole (DAPI) was purchased from Sigma-Aldrich (Saint Louis, MO). Cy5-labeled anti-miR-21 RNA-oligo was synthesized from the Protein and Nucleic Acid facility at Stanford (PAN).

Methods.—The mouse breast cancer cells (4T1), human breast cancer cells (SKBR3), human glioblastoma cells (U87MG, Ln229 and Ln308), human hepatocellular carcinoma cells (HepG2), human ovarian carcinoma cells (HEY), and human embryonic kidney cells

(HEK293T) were purchased from the American Type Culture Collection (ATCC, Manassas, VA) and cultured in accordance with the supplier's instructions.

Transfection ofCy5-anti-miR-21 RNA Oligo into the Donor Cells.—For the efficient loading of Cy5-anti-miR-21 into donor cells derived EVs, we plated different cells (4T1, SKBR3, HepG2) to 70% confluence (4×10^6 cells per 10 cm plate) 24 h before transfection. After 24 h, the cells were washed once with PBS, and we added 8 mL of fresh medium. For transfection, 5 nmol of Cy5-anti-miR-21 was complexed with 25 μL of Lipofectamine 2000 transfection reagent in 1 mL of serum-free optiMEM as per the manufacturer's instructions. After 45 min of incubation at room temperature in the dark, the complex was mixed well and added to the plates. After 16 h of transfection, the plates were washed once with PBS, and we added 8 mL of serum-free DMEM with penicillin and streptomycin for 24 h. The plates were kept in a shaker (300 rpm) for additional 12 h for the release of EVs. The medium was collected and used for tumor derived extracellular vesicles (TEVs) isolation as described below.

Isolation of Tumor-Derived Extracellular Vesicles.—TEVs were harvested by a modified protocol.[34] Briefly, conditioned medium was centrifuged at 300*g* for 30 min to remove cells and debris. The supernatant was further centrifuged again at 2000*g* for 30 min to remove apoptotic bodies. Total TEVs were collected by ultracentrifugation at 250000g for 120 min using Sorvall centrifuge with a SureSpin rotor (Thermo Fisher Scientific). The pellet was carefully suspended in the required volume of PBS and used for further characterization and studies.

Characterization of EVs by Fluorescent Microscopy and FACS Analysis.—The TEVs isolated from 4T1 cells transfected with Cy5-anti-miR-21 were evaluated for anti-miR-21 loading by indirectly measuring Cy5-fluorescence in EVs by fluorescence microscope and FACS analysis. For fluorescence microscopy, 5 μL of EVs isolated from cells at a concentration of 6 × 10 cells per milliliter was placed on a glass slide, and a coverslip was placed without generating any air bubbles. The slide was imaged for EVs with Cy5 fluorescence using Olympus iX81 fluorescence microscopy with a 40× oil immersion lens. Similarly, for FACS analysis, we used 100 μL of EVs at 6×10^{10} EVs/mL. The Guava easyCyte Flow Cytometer from Millipore was used for analysis. The optimal window for analysis was set by using PBS to eliminate debris, and negative EVs were used to set compensation and Cy5-anti-miR-21 loaded EVs as positive samples. We collected 25 000 events from each sample for analysis. The results were analyzed using FlowJo 8.6.6 Software for EVs based on their fluorescence intensities.

Preparation of Tumor-Derived Extracellular Vesicles Coated Gold-Iron Oxide Nanotheranostics.—We have adopted the top-down method for the preparation of tumor-derived extracellular vesicle coated gold–iron oxide NPs.[18] The preformulated GION cores were co-extruded with TEVs through a 200 nm pore sized polycarbonate membrane with TEV to GION at a ratio of 1:15 for 7 to 11 passes and then purified by centrifugation at 3000 rpm for 30 min to exclude GIONs without TEVs. The extruded TEVs-GIONs were further characterized by electron microscope. The mixture ratio was optimized with the

surface area calculation as described previously,[18] and the particles were passed through the extruder repeatedly to ensure that the particles were completely coated with a homogeneous lipid shell.

Characterization of TEVs-GIONs UV-Vis Spectroscopy.—To evaluate the presence of magnetic core in the TEVs-GIONs, in the first step, an external magnet was used to separate TEVs-GIONs from plain TEVs. The separated GIONs, TEVs, and TEVs-GIONs were then suspended in DI water and analyzed by UV–vis spectroscopy by scanning from 400 to 700 nm in spectrophotometer (Infiniti1000, Tecan-Safire).

ζ Potential, DLS, and Nanoparticle-Tracking Analysis.—The mean particle diameter (*z* average), size distribution (polydispersity index), and the surface charge (the ζ potential) of GIONs, TEV, and TEVs-GIONs were determined using a Zetasizer NanoZS (Malvern Instruments, Malvern, UK). For DLS measurements, the samples were diluted in 18.2 MΩ water, and the data from at least three measurements were averaged. The ζ potential was measured at pH 7.4. The data were processed using the absorption of bulk iron oxide, the indices of refraction of iron oxide and solvent, and the viscosity of the pure water. The Smoluchowski approximation was used to convert the electrophoretic mobility to a ζ potential.

For NTA analysis, GIONs, TEVs, and the TEVs-GIONs were further diluted 100-fold to 1000-fold for the measurement of particle size and concentration in the media. All NTA measurements were carried out using the Nano sight NS300 (Malvern Instruments). For each sample, at least 5 videos of 30–60 s with more than 200 detected tracks per video, and in at least one dilution, were taken and analyzed using the Nanoparticle Tracking Analysis software with the default settings.

Transmission Electron Microscopy and Energy-Dispersive X-ray Spectra Analysis.—Transmission electron microscopy (TEM) images of the GIONs, TEVs, and TEVs-GIONs were carried out using a FEI-Tecnai G2 F20 X-TWIN instrument that was operated at an acceleration voltage of 200 kV. Images were taken on an ORIUS CCD camera through Digital Micrograph, and energy dispersive X-ray spectra (EDS) were recorded through the FEI-TIA interface. For sample preparation, 10 μL of GIONs, TEVs, and TEVs-GIONs suspension were drop-cast on glow discharged copper grids with pure carbon support film and incubated for 10–15 min and then washed with ultrapure water. Finally, the sample grids were negatively stained with 1% uranyl acetate solution.

SDS-PAGE Analysis.—The protein concentrations of TEVs were estimated using a Pierce 660 protein assay kit (Life Technologies, CA), and then 25 μg of protein was denatured in SDS sample buffer (Invitrogen, Carlsbad, CA). The samples were then resolved in a NuPAGE Novex 4–12% Bis–Tris 10-well mini gel in 3-(*N*- morpholino) propanesulfonic acid running buffer using Novex-SureLock-Xcell Electrophoresis System (Invitrogen). The gel was stained in SimplyBlue (Invitrogen) staining buffer for 1 h and further washed in water for destaining and visualization of target protein bands.

Immunoblot Analysis.—Important TEVs-associated proteins were immunoblot analyzed after resolving the protein in SDS-PAGE. We used a Novex ExCell Sure-Lock SDS-PAGE Electrophoresis System (Life Technologies, Carlsbad, CA). Briefly, 50 μg protein samples obtained from TEVs were reduced and denatured in sample buffer and then electrophoresed on a 4% to 12% Tris gradient gel with Tris running buffer, blotted to a polyvinylidene fluoride membrane using a wet-transfer system, and probed with primary antibodies against ZO1, E-Cadherin, Histone 3, H3K9me3, and H3K27me3 (Cell Signaling, Danver, MA). A horseradish-peroxidase (HRP)-conjugated anti-rabbit or anti-mouse secondary antibody (Cell Signaling, Danver, MA) was then added, which was detected by using enhanced Chemiluminescence (ECL Plus, GE Healthcare, Milwaukee, WI) system in an IVIS optical imaging system (PerkinElmer, Waltham, MA).

Confirmation of Functional Effects of miRNA by Immunoblot Analysis.—For the immunoblot assay, we used the protocol described in our previous work.[6] Briefly, for assessing the functional effects of anti-miR-21 in cells delivered with TEVs, we assessed Bcl2, PTEN, PDCD4, and GAPDH expression in recipient 4T1 cells after respective treatment conditions (with donor4T1-TEVs-Cy5-anti-miR-21)for48 h. The cells were collected after treatment and lysed by mild sonication in PBS buffer containing protease inhibitor cocktail. The cell lysates were incubated for 1 h in an ice bath and vortex-mixed for every 15 min for 5 s and centrifuged at 14 000 rpm at 4 °C for 15 min. As discussed above, the SDS-PAGE and immunoblotting was performed, and then the respective primary rabbit antibodies for PTEN, PDCD4, Bcl2, and GAPDH were added. The HRP-conjugated anti-rabbit or anti-mouse antibody (1:5000) was used for detection. Chemiluminescent HRP substrate LuminoGlo (Cell Signaling, Beverly, MA) was added to the membrane and imaged with an IVIS—Lumina imaging system. Images were analyzed by IVIS—Lumina Image software.

Proteomic Analysis.—The protein samples were digested overnight at 37 °C following the addition of 1 μg of trypsin per 20 μg of protein, and the tryptic peptide samples were reconstituted in 15 μL of 0.1% formic acid in water. Approximately 10 μg (8 μL samples) of protein from each sample was injected onto a C18 PepMap100 trap column using an UltiMate Rapid Separation liquid chromatography system (Dionex) with a flow rate of 5 μL/min 0.1% formic acid in water. Peptides were then separated by reverse-phase chromatography on a 25 cm long C18 analytical column packed in-house with Magic C18AQ (Michrom Bioresources). A multistep gradient protocol was used to elute peptides from the column, and the eluted peptides were used for LC—MS/MS analysis using a LTQ-Velos Orbitrap mass spectrometer (Thermo Fisher Scientific). MS1 scan resolution and range were set to 6 000 and m/z = 400—1800, respectively. TheAGC targetvaluewas setto 1 × 10^6. The top 10 most abundant ions in each MS1 scan were selected for collision-induced dissociation (35 eV). The MS2 AGC target value was set to 3 × 10^4, and dynamic exclusion was enabled for 30 s. Data were searched using Byonic (Protein Metrics) against the UniProt database using the following parameters: maximum number of missed cleavages, 2; precursor tolerance, 10 ppm; oxidation at methionine, common modification; deamidation of asparagine, rare modification; and false discovery rate, <1%. Quantitation was performed by peptide (spectral counts).

RNA Extraction and qRT-PCR Analysis.—Author: Total RNA was extracted from TEVs using mirVana RNA extraction kit (Life technologies, Grand Island, NY) as per the manufacturer's protocol. In brief, the TEVs (250 μg) or cells transfected with TEVs of different concentrations(5, 10, 15, 20, 25, and 30μg) or tissues of different organs were lysed and homogenized in 300 μL oflysis buffer for 3 min. The lysis buffer was supplemented with 30 μL of homogenate additive and incubated at RT for 10 min. The RNA was extracted once with phenol and chloroform and purified using a column, washed with wash buffer, and eluted in 50 μL of sterile distilled water. The total RNA was quantified and checked for purity using a Nanodrop spectrophotometer. After quantification, 15 ng of total RNA was reverse-transcribed using RT primers (Life Technologies) using a reverse-transcription kit (Life technologies) to produce corresponding cDNA. The cDNA synthesis was carried out in a 15 μL reaction volume. qRT-PCR was performed using cDNA (5 ng of RNA equivalent) combined with TaqMan-PCR reagents (primer and probe mix). qRT-PCRwas performed by 2 min of incubation at 50 °C followed by activation of the DNA polymerase at 95 °C for 10 min, 60 cycles of 95 °C for 15 s, and 60 °C for 60 s in an Eppendorf Real flex qRT-PCR system (Eppendorf AG, Hamburg, Germany). The qRT-PCR reaction was carried out in a 20 μL reaction volume. The expression of miRNA was calculated using the $2^{-\Delta CT}$ method.

Analysis of Cellular Uptake of Cy5-anti-miRNA-21-Loaded TEVs.—Initially, we investigated the homologues cell uptake efficiency of TEVs derived from 4T1 cells (donor) in 4T1 cells (recipient). For this purpose, the 4T1 cells (5×10^3 cells per well) plated in 96-well plates were incubated with 5 μg of 4T1 cells derived Cy5-AnitmiRNA loaded TEVs for 48 h at 37 °C with 5% CO_2. After incubation, the cells were used for direct visualization under fluorescent microscope or fixed in 4% PFA in PBS for 10 min, washed in PBS, permeabilized with Triton-X, and stained with 3 μM DAPI for 2 min, and then visualized with an Olympus IX 81 fluorescent microscope. The same procedure was used for measuring the cellular uptake of TEVs-GION in 4T1 cells. We also examined the time-and concentration-dependent homologues cancer cell uptake of TEV. For concentration-dependent uptake, the recipient 4T1 cells were treated with different concentration (5, 10, and 15 μL) of 4T1-derived TEVs in 100 μL of medium. After 48 h, the Cy5 fluorescence images were captured. For time-dependent uptake, the recipient 4T1 cells were treated with 10 μLof 4T1-derived TEVs. After 24, 48, and 72 h, the Cy5 fluorescence images were acquired.

Cancer-cell-derived vesicles have various surface proteins that play a vital role in homologues and heterologous adhesions. Therefore, we also examined the heterologous cells uptake efficiency using cross-transfection. For this purpose, the mouse and human breast cancer cell lines (4T1 and SKBR3), and human hepatocellular carcinoma cells (5×10^3) were grown on 96-well plates for 24 h and were treated with 15 μg of Cy5-anti-miRNA-21 TEVs (based on the protein quantification) derived from 4T1, SKBR3, and HepG2, respectively, for 48 h at 37 °C with 5% CO_2. After 48 h ofincubation, these cells were washed with PBS and then visualized using Olympus 81X fluorescence microscope. Additionally, the diverse cancer cell uptake ofTEVs were also quantified by Guava easyCyte Flow Cytometer and analyzed using FlowJo software.

To further investigate the migration and selective adhesion properties of TEVs, we tested 4T1-derived TEVs immobilized in matrigel to a diverse group of human cancer cells of different origin (ovarian, Hey cells; glioblastoma, U87MG, Ln-308, and Ln229; HCC, HepG2; and immortalized control, HEK293T). First, we studied the TEVs uptake by source cell (4T1). After 48 h oftreatment, the migration and adhesion of TEVs-Cy5-anti-miRNA-21 were visualized by Olympus 81X fluorescence microscope.

Chemosensitizing EffectofTEV-anti-miR-21 on 4T1 Cells byFACS Analysis.—To investigate the chemosensitizing effect of TEV-AmiRNA- 21, the 4T1 cells were seeded at a density of1×10^5 cells per well in 12-well plates. Next, the cells were transfected with TEV-anti-miRNA-21 for 24 h and treated with DOX in different concentrations (0.25,0.5, and 1.0 μM) for another 48 h. The cells were collected and fixed in ice cold 70% ethanol at — 20 C for 2h. The fixed cells collected by centrifugation at 2000 rpm for 5 min. The cells were washed once with 2 mL of PBS and used for propidium iodide (PI) staining. Briefly, cells were resuspended in 0.5 mL of PBS/RNase A (10 μg/mL)/Triton X-100 (0.1%) buffer containing 0.5 μg/mL of PI. After 15 min of incubation at room temperature in the dark, cells were washed once with PBS and subjected to FACS analysis (Guava). The generated data were analyzed byFlowJo 8.6.6 Software for live and dead cells and for cell-cycle status analysis.

For cell-cycle analysis, the same cells stained with PI mentioned above was analyzed in a Guava easyCyte flow cytometer using a cell-cycle analysis program that is set with windows based on DNA content and collected a minimum 5000 cells for each sample. The results were analyzed using FlowJo 8.6.6 Software for cells based on different cell-cycle status and compared with controls.

TEVand TEV-GIONs Uptake Studies in RAW264.7Cells.—RAW 264.7 cells were purchased from ATCC and propagated, and aliquots were stored in liquid nitrogen. Cells were maintained as adherent cell cultures and passaged three times, after which a new frozen aliquot was used. Cell treatments were performed in adherent conditions. The RAW 264.7 cell densityof 1×10^5 cells per well in 12-well plates were treated with TEV- Cy5-anti-miR-21 and TEV-Cy5-anti-miR-21-GION at6×10^9 EVs/mL for treatment. The cells treated with cationic liposome labeled with DiD at similar concentrations were used as a positive control. After 24 h of treatment, the cells were imaged for EV uptake in RAW 264.7 cells by fluorescence microscopy for the Cy5-anti-miR-21 and DiD. The cells stained with DAPI nuclear stain was used to localize cells.

Photothermal Therapy.—For *in vitro* photothermal ablation experiments 4T1 cells were seeded in 24-well dishes. Before the experiments, the cells were randomly distributed and treated as follows: group 1 was the untreated control, group 2 received only TEVs isolated from naive cells, group 3 received TEVs-Cy5-anti-miRNA-21, group 4 received TEVs-GIONs (without Cy5-anti-miRNA-21), and group 5 received TEVs-Cy5-anti-miRNA-21. Groups 6 and 7 were negative-control groups without NIR irradiation. The experimental groups were irradiated with 980 nm laser for 15 min at 0.35 W cm^{-2}. In this experiment, the apoptosis was measured by PI staining of cells of each group after treatment. The

photothermal ablation results were captured using fluorescence microscopy and quantified via flow cytometry.

For staining live cells in plates, after the completion of respective treatment periods, the cells were treated with 10 μg/mL of PI in the medium for 15 min and gently washed once, and fresh medium was added before they were used for obtaining fluorescence microscopic images in a Texas Red filter set using an Olympus ix81 fluorescent microscope.

In Vivo Biodistribution andin VivoAntitumorActivityStudies with TEV-GION and TEV-GION-anti-miR-21.—The 4T1-syngeneic subcutaneous breast tumor model was established by injecting 0.1 mL of 4T1-Fluc-eGFP cell suspension (5×10^6) into the left and right flanks of female nude mice (nu/nu) using 50% (v/v) Matrigel. After 2 weeks, when the tumors grew to 100–300 mm^3 size, the animals were randomly assigned into two groups (1, TEV-GION; and 2, TEV-GION-anti-miRNA-21). For the preparation of ICG-labeled TEV-GION and TEV-GION-anti-miR-21, we used a chemical conjugation process. Briefly, the NH2-reactive ICG (125 μg) was mixed with 875 μg of protein equivalent of TEV/TEV-anti-miR-21 (1:7 dye to protein ratio; 2×10^{12} EV equivalent) in 1 mL of 100 mM sodium bicarbonate buffer and kept in a shaker for 1 h with a constant mixing. After 1 h, the ICG-conjugated TEV or TEV-anti-miR-21 was extruded with GIONs. Finally, the excess of ICG from TEVs was washed twice in PBS buffer by centrifugation, as mentioned earlier. To investigate the labeling efficiency of TEVs, the TEV-GIONs were resolved in SDS-PAGE and viewed under an IVIS optical imaging system using ICG filter. We also used a fluorescent microscope and a Cy7 filter to view ICG fluorescence from intact TEVs. Similarly, the Alexa 633 labeled TEVs prepared using the same protocol were assessed by FACS analysis. Prior to TEV-GION-ICG or TEV-GION-antmiRNA-21-ICG injection, mice bearing 4T1 tumors were anesthetized and administered with 100 μL of D-luciferin (30 mg/mL in PBS) via intraperitoneal injection and assessed by a Lago Spectral Imaging system for bioluminescence and near-infrared fluorescence (NIRF) signals. At every time point, tumor volumes were measured and imaged using a Lago Spectral Imaging system; after imaging, animals were systemically administered with 150 μL of TEV-GION-ICG or TEV-GION-anti-miRNA-21-ICG (3×10^{11} particles) on days 1, 4, and 8 and imaged using a Lago Spectral Imaging system on days 0, 1, 2, 4, 6, 8, and 12 for fluorescence. In parallel, free ICG was administered in separate healthy mice and imaged using a Lago Spectral Imaging Instrument as a control for biodistribution. All animals were treated with 5 mg/kg DOX on day 0, 1, 2, 4, 6, 8, and 10. Finally all the animals were sacrificed and the organs (liver, spleen, kidney, heart, lungs, and brain) and tumors were collected from all animals and used for *ex vivo* analysis. For anti-miR-21 biodistribution in different organs, we used Taqman real-time qRT-PCR following the protocol mentioned earlier. We used mouse sno234 miRNA as housekeeping miRNA for normalization.

MR Imaging.—The *in vitro* and *in vivo* MRI contrast enhancement effect of TEV-GION was measured using a 3T MRI scanner (MR Solutions Ltd., Guildford, UK). For in vitro study, MRI samples of 4T1 cells with various formulations (controls and experimental samples) were prepared in small plastic dishes. Standard T1- and T2-weighted MRI scans were performed using a mouse body coil (MR Solutions Ltd.). For *in vivo* study, TEV-

GION-ICG or TEV-GION-AmiRNA21 were systemicallyadministered as mentioned early, and the animals were imaged at day 12. Standard T1- and T2-weighted MRI scans were acquired, and the images were transferred to a local workstation and analyzed using a commercial 3D analysis software “Inveon Research Workplace (IRW)” (Siemens Health Care, Knoxville, TN).

Statistical Analyses.—Student’s *t* test was performed for all statistical analyses. *P* values are indicated. Differences were considered to be statistically significant when the *P* value was less than 0.05.

Supplementary Material

Refer to Web version on PubMed Central for supplementary material.

ACKNOWLEDGMENTS

We thank the Canary Center at Stanford Department of Radiology for facility and resources. We also thank the SCi^3 small-animal imaging service center at the Stanford University School of Medicine for providing imaging facilities and data-analysis support.

Funding

This research was supported by National Institutes of Health (NIH) grant nos. R01CA209888 and R21EB022298, the Focused Ultrasound Society, and the Ben and Catherine Ivy Foundation. This work was also supported by the Center for Cancer Nanotechnology Excellence for Translational Diagnostics (CCNE-TD) at Stanford University through an award (grant no. U54 CA199075) from the National Cancer Institute of the NIH.

REFERENCES

(1). Bartel DP MicroRNAs: Target Recognition and Regulatory Functions. Cell 2009, 136, 215–233. [PubMed: 19167326]

(2). Kurozumi S; Yamaguchi Y; Kurosumi M; Ohira M; Matsumoto H; Horiguchi J Recent Trends in Microrna Research into Breast Cancer with Particular Focus on the Associations Between Micrornas and Intrinsic Subtypes. J. Hum. Genet. 2017, 62, 15–24. [PubMed: 27439682]

(3). Barata P; Sood AK; Hong DS RNA-Targeted Therapeutics in Cancer Clinical Trials: Current Status and Future Directions. Cancer Treat. Rev. 2016, 50, 35–47. [PubMed: 27612280]

(4). Rupaimoole R; Slack FJ Microrna Therapeutics: Towards a New Era for the Management of Cancer and Other Diseases. Nat. Rev. Drug Discovery 2017, 16, 203–222. [PubMed: 28209991]

(5). Beierlein JM; McNamee LM; Ledley FD As Technologies for Nucleotide Therapeutics Mature, Products Emerge. Mol. Ther.--Nucleic Acids 2017, 9, 379–386. [PubMed: 29246316]

(6). Devulapally R; Foygel K; Sekar TV; Willmann JK; Paulmurugan R Gemcitabine and Antisense-microRNA Co-encapsulated PLGA-PEG Polymer Nanoparticles for Hepatocellular Carcinoma Therapy. ACS Appl. Mater. Interfaces 2016, 8, 33412–33422. [PubMed: 27960411]

(7). Liu J; Ma J; Tang K; Huang B Therapeutic Use ofTumor Cell- DerivedExtracellularVesicles. Methods Mol. Biol. 2017,1660,433–440. [PubMed: 28828677]

(8). Pfeffer SR; Yang CH; Pfeffer LM The Role of miR-21 in Cancer. Drug Dev. Res. 2015, 76, 270–277. [PubMed: 26082192]

(9). Devulapally R; Sekar NM; Sekar TV; Foygel K; Massoud TF; Willmann JK; Paulmurugan R Polymer Nanoparticles Mediated Codelivery of Antimir-10b and Antimir-21 for Achieving Triple Negative Breast Cancer Therapy. ACS Nano 2015, 9, 2290–2302. [PubMed: 25652012]

(10). Mullick Chowdhury S; Wang TY; Bachawal S; Devulapally R; Choe JW; Abou Elkacem L; Yakub BK; Wang DS; Tian L; Paulmurugan R; Willmann JK Ultrasound-Guided Therapeutic

Modulation of Hepatocellular Carcinoma Using Complementary Micrornas. J. Controlled Release 2016, 238, 272–280.

(11). Ananta JS; Paulmurugan R; Massoud TF Nanoparticle-Delivered Antisense MicroRNA-21 Enhances the Effects of Temozo-lomide on Glioblastoma Cells. Mol. Pharmaceutics 2015, 12, 4509–4517.

(12). Gaudelot K; Gibier JB; Pottier N; Hemon B;Van Seuningen I; Glowacki F; Leroy X; Cauffiez C; Gnemmi V; Aubert S; Perrais M Targeting Mir-21 Decreases Expression of Multi-Drug Resistant Genes and Promotes ChemosensitivityofRenal Carcinoma. Tumor Biol. 2017, 39, 1.

(13). Chen H; Zhang W; Zhu G; Xie J; Chen X RethinkingCancer Nanotheranostics. Nat. Rev. Mater. 2017, 2, 17024. [PubMed: 29075517]

(14). Webb JA; Ou YC; Faley S; Paul EP; Hittinger JP; Cutright CC; Lin EC; Bellan LM; Bardhan R Theranostic Gold Nanoantennas for Simultaneous Multiplexed Raman Imaging of Immunomarkers and Photothermal Therapy. ACS Omega 2017, 2, 3583–3594. [PubMed: 28782050]

(15). Azhdarzadeh M; Atyabi F; Saei AA; Varnamkhasti BS; Omidi Y; Fateh M; Ghavami M; Shanehsazzadeh S; Dinarvand R Theranostic MUC-1 Aptamer Targeted Gold Coated Superparamag-netic Iron Oxide Nanoparticles for Magnetic Resonance Imaging and Photothermal Therapy of Colon Cancer. Colloids Surf. B 2016, 143, 224–232.

(16). Reguera J; Jimenez de Aberasturi D; Henriksen-Lacey M; Langer J; Espinosa A; Szczupak B; Wilhelm C; Liz-Marzan LM Janus Plasmonic-Magnetic Gold-Iron Oxide Nanoparticles as Contrast Agents for Multimodal Imaging. Nanoscale 2017, 9, 9467–9480. [PubMed: 28660946]

(17). Riley RS; Day ES GoldNanoparticle-Mediated Photothermal Therapy: Applications and Opportunities for Multimodal Cancer Treatment. Wiley Interdiscip Rev. Nanomed Nanobiotechnol 2017, 9, 1 DOI: 10.1002/wnan.1449.

(18). Gao W; Hu CM; Fang RH; Luk BT; Su J; Zhang L Surface Functionalization of Gold Nanoparticles with Red Blood Cell Membranes. Adv. Mater. 2013, 25, 3549–3553. [PubMed: 23712782]

(19). Bose RJ; Lee SH; Park H Biofunctionalized Nanoparticles: An Emerging Drug Delivery Platform for Various Disease Treatments. Drug Discovery Today 2016, 21, 1303–1312. [PubMed: 27297732]

(20). Bose RJC; Paulmurugan R; Moon J; Lee SH; Park H Cell Membrane-Coated Nanocarriers: The Emerging Targeted Delivery System for Cancer Theranostics. Drug Discovery Today 2018, 23, 891–899. [PubMed: 29426004]

(21). Lamichhane TN; Raiker RS; Jay SM Exogenous DNA Loading into Extracellular Vesicles via Electroporation is Size-Dependent and Enables Limited Gene Delivery. Mol. Pharmaceutics 2015, 12, 3650–3657.

(22). Sutaria DS; Jiang J; Elgamal OA; Pomeroy SM; Badawi M; Zhu X; Pavlovicz R; Azevedo-Pouly ACP; Chalmers J; Li C; Phelps MA; Schmittgen TD Low Active Loading of Cargo into Engineered Extracellular Vesicles Results in Inefficient Mirna Mimic Delivery. J. Extracell. Vesicles 2017, 6, 1333882.

(23). Christianson HC; Svensson KJ; van Kuppevelt TH; Li JP; Belting M Cancer Cell Exosomes Depend on Cell-Surface Heparan Sulfate Proteoglycans for their Internalization and Functional Activity. Proc. Natl. Acad. Sci. U. S. A. 2013, 110, 17380–17385. [PubMed: 24101524]

(24). Fang RH; Jiang Y; Fang JC; Zhang L Cell Membrane-Derived Nanomaterials for Biomedical Applications. Biomaterials 2017, 128, 69–83. [PubMed: 28292726]

(25). Fehon RG; McClatchey AI; Bretscher A Organizingthe Cell Cortex: The Role of ERM Proteins. Nat. Rev. Mol. Cell Biol. 2010, 11, 276–287. [PubMed: 20308985]

(26). Sun H; Su J; Meng Q; Yin Q; Chen L; Gu W; Zhang P; Zhang Z; Yu H; Wang S; et al. Cancer-Cell-Biomimetic Nanoparticles for Targeted Therapy of HomotypicTumors. Adv. Mater. 2016, 28, 9581–9588. [PubMed: 27628433]

(27). England CG; Priest T; Zhang G; Sun X; Patel DN; McNally LR; van Berkel V; Gobin AM; Frieboes HB Enhanced Penetration into 3D Cell Culture using Two and Three Layered Gold Nanoparticles. Int. J. Nanomed. 2013, 8, 3603–3617.

(28). Chen B; Le W; Wang Y; Li Z; Wang D; Lin L; Cui S; Hu JJ; Hu Y; Yang P; Ewing RC; Shi D; Cui Z Targeting Negative Surface Charges of Cancer Cells by Multifunctional Nanoprobes. Theranostics 2016, 6, 1887–1898. [PubMed: 27570558]

(29). Mendes R; Pedrosa P; Lima JC; Fernandes AR; Baptista PV Photothermal Enhancement of Chemotherapy in Breast Cancer by Visible Irradiation of Gold Nanoparticles. Sci. Rep. 2017, 7, 10872. [PubMed: 28883606]

(30). Dou QQ; Rengaramchandran A; Selvan ST; Paulmurugan R; Zhang Y Core-Shell Upconversion Nanoparticle - Semiconductor Heterostructures for Photodynamic Therapy. Sci. Rep. 2015, 5, 8252. [PubMed: 25652742]

(31). Fernandez Cabada T; Sanchez Lopez de Pablo C; Martinez Serrano A; del Pozo Guerrero F; Serrano Olmedo JJ; Ramos Gomez M Induction of Cell Death in a Glioblastoma Line by Hyperthermic TherapyBased on Gold Nanorods. Int. J. Nanomedicine 2012, 7, 1511–1523. [PubMed: 22619509]

(32). Hoshino A; Costa-Silva B; Shen TL; Rodrigues G; Hashimoto A; Tesic Mark M; Molina H; Kohsaka S; Di Giannatale A; Ceder S; Singh S; Williams C; Soplop N; Uryu K; Pharmer L; King T; Bojmar L; Davies AE; Ararso Y; Zhang T; et al.et al. Tumour Exosome Integrins Determine Organotropic Metastasis. Nature 2015, 527, 329–335. [PubMed: 26524530]

(33). Bourguignon LY; Spevak CC; Wong G; Xia W; Gilad E Hyaluronan-CD44 Interaction with Protein Kinase C(Epsilon) Promotes Oncogenic Signaling by the Stem Cell Marker Nanog and the Production of Microrna-21, Leading to Down-Regulation of the Tumor Suppressor Protein PDCD4, Anti-Apoptosis, and Chemotherapy Resistance in Breast Tumor Cells. J. Biol. Chem. 2009, 284, 26533–26546. [PubMed: 19633292]

(34). Kanada M; Bachmann MH; Hardy JW; Frimannson DO; Bronsart L; Wang A; Sylvester MD; Schmidt TL; Kaspar RL; Butte MJ; Matin AC; Contag CH Differential Fates of Biomolecules Delivered to Target Cells via Extracellular Vesicles. Proc. Natl. Acad. Sci. U. S. A. 2015, 112, E1433–1442. [PubMed: 25713383]

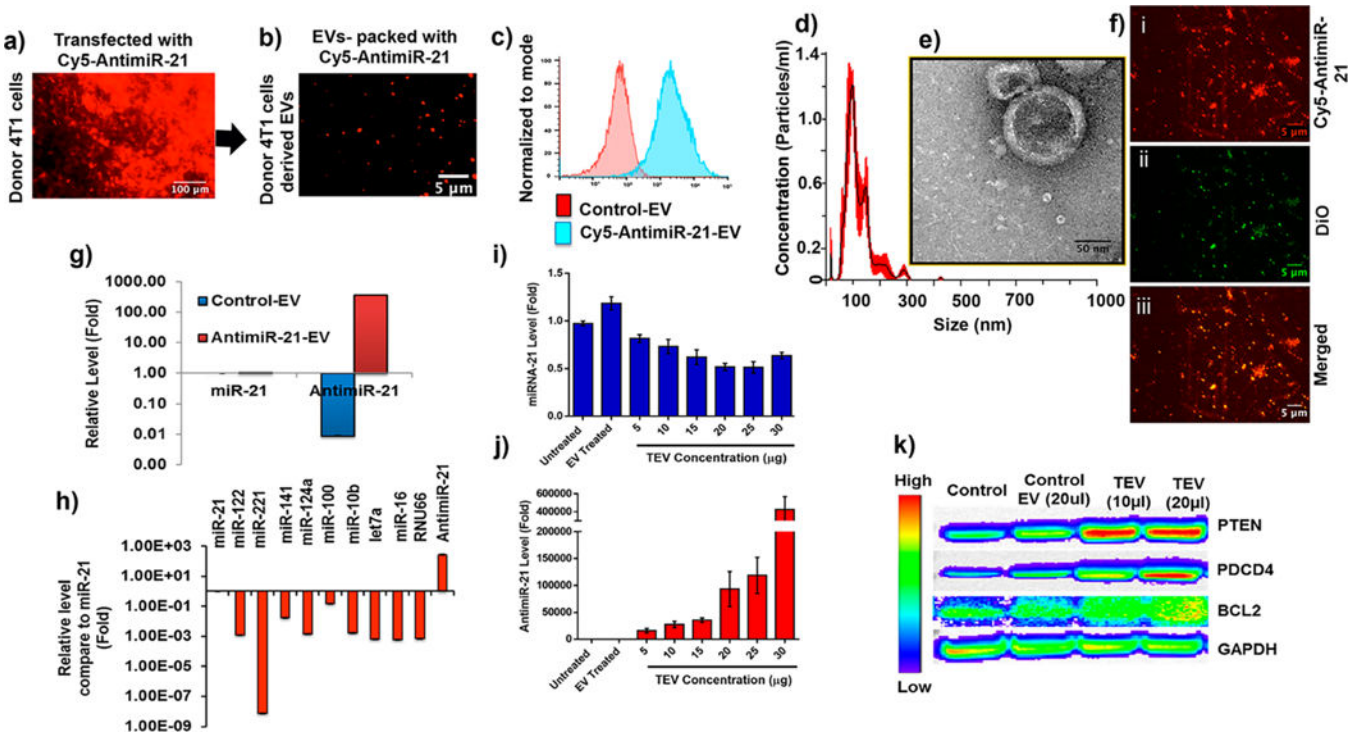

Figure 1.

TEVs preparation and characterization. Fluorescence microscopy images showing: (a) transient transfection of Cy5-anti-miRNA-21 into the donor 4T1 cells; (b) Cy5-anti-miRNA-21-packed donor 4T1 cell derived TEVs; (c) flow-cytometry analysis of Cy5-anti-miRNA-21 packed donor 4T1 cell derived TEVs; (d) size distribution of TEVs packed with Cy5-anti-miRNA-21 measured by NTA; (e) transmission electron microscopy image of 4T1-TEVs (scale bar: 50 nm); (f) fluorescence microscopy images showing 4T1-TEVs packed with Cy5-antimiRNA- 21 (red), labeled with DiO (green), and merged images of DiO-labeled TEVs packed with Cy5-anti-miRNA-21; (g) quantification of packed anti-miRNA-21 and endogenous miRNA-21 in donor and naive 4T1 cell derived TEVs by qRT-PCR; (h) quantification of selective endogenous miRNAs profile in TEVs purified from donor 4T1 cells; (i) quantification of endogenous miRNA-21 level in 4T1 cells delivered by different concentrations of Cy5-anti-miRNA-21 TEVs; (j) quantification of endogenous anti-miRNA-21 level in 4T1 cells delivered by different concentration of Cy5-anti-miRNA-21 TEVs; and (k) Western blot analysis showing the expression of therapeutic miRNA target proteins (PTEN, PDCD4, and Bcl2) in 4T1 cells transfected with Cy5-anti-miRNA-21 TEVs.

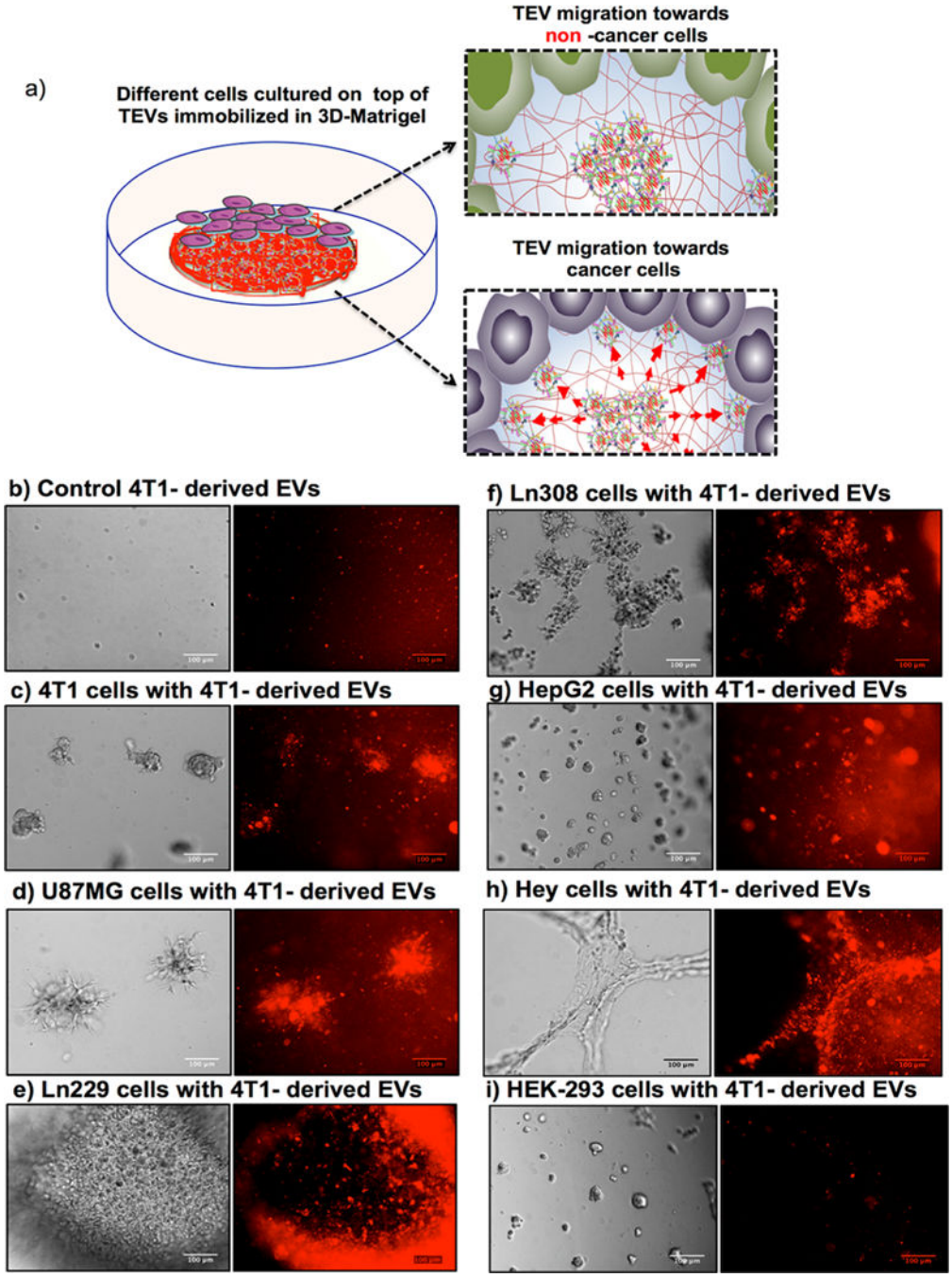

Figure 2.

4T1-derived EV-mediated Cy5-anti-miRNA-21 delivery in various types of cancer cells. (a) Schematic diagram details the design of the experiment, (b) control 4T1-derived EVs, (c) recipient 4T1 cells transfected with donor 4T1-derived EVs, (d) U87-MG cells transfected with donor 4T1 derived EVs, (e) Ln229 cells transfected with donor 4T1-derived EVs, (f) Ln308 cells transfected with donor 4T1-derived EVs, (g) HepG2 cells transfected with donor 4T1 derived EVs, (h) Hey cells transfected with donor 4T1-derived EVs, and (i) HEK-293T cells transfected with donor 4T1-derived EVs (scale bar: 100 μM).

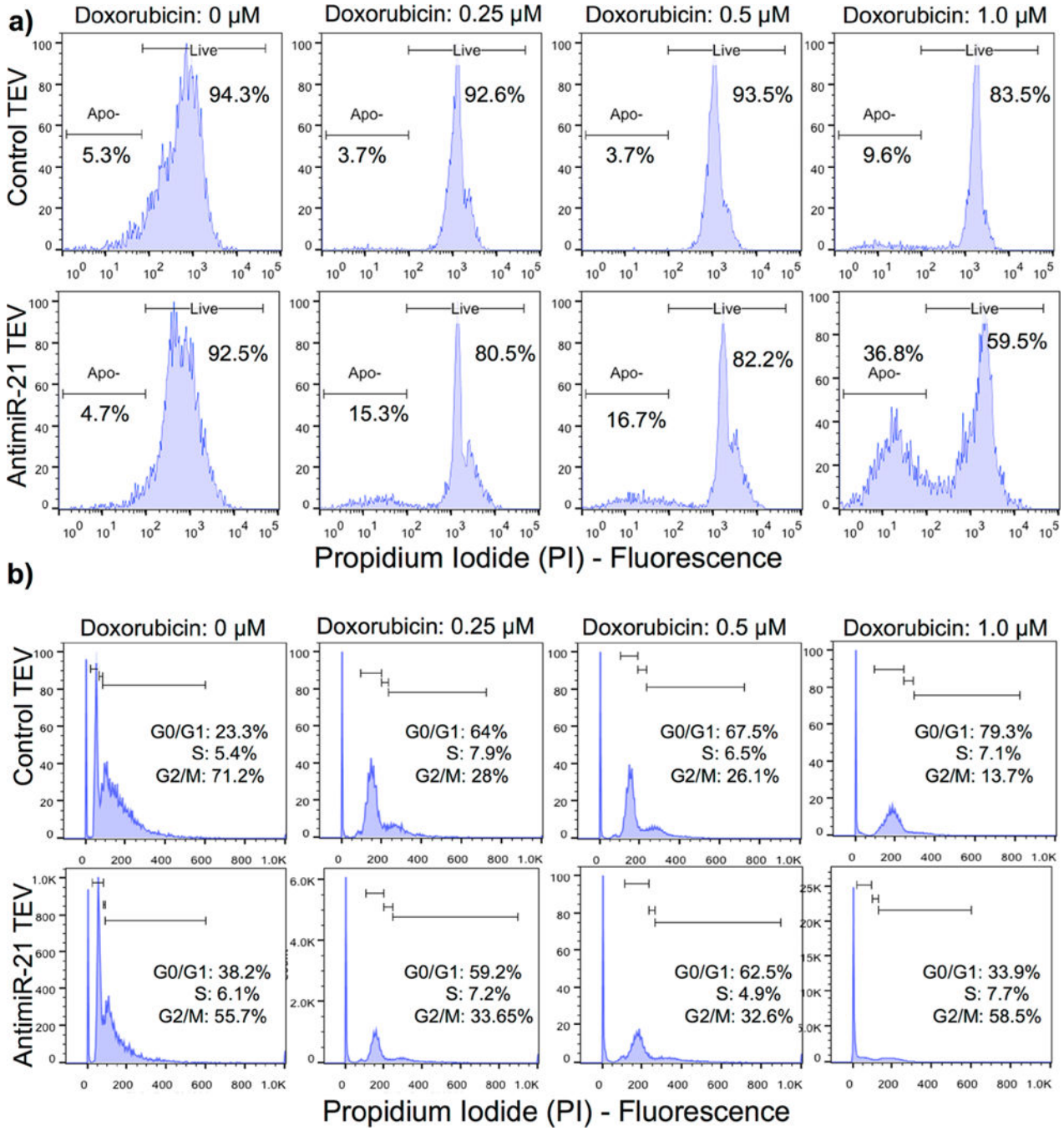

Figure 3.

Chemosensitizing effect of TEVs-anti-miR-21 evaluated in 4T1 cancer cells co-treated with doxorubicin. (a) PI-staining-based FACS analysis of 4T1 cells treated or co-treated with control EV and TEVs-anti-miR-21 in the presence of different concentrations of doxorubicin measured for the induced live and apoptotic cell populations. (b) Cell cycle analysis of samples shown in panel “a” for measuring cells arrested at different stages in response to the treatment with doxorubicin in the presence of control EVs or TEVs-anti-miR-21.

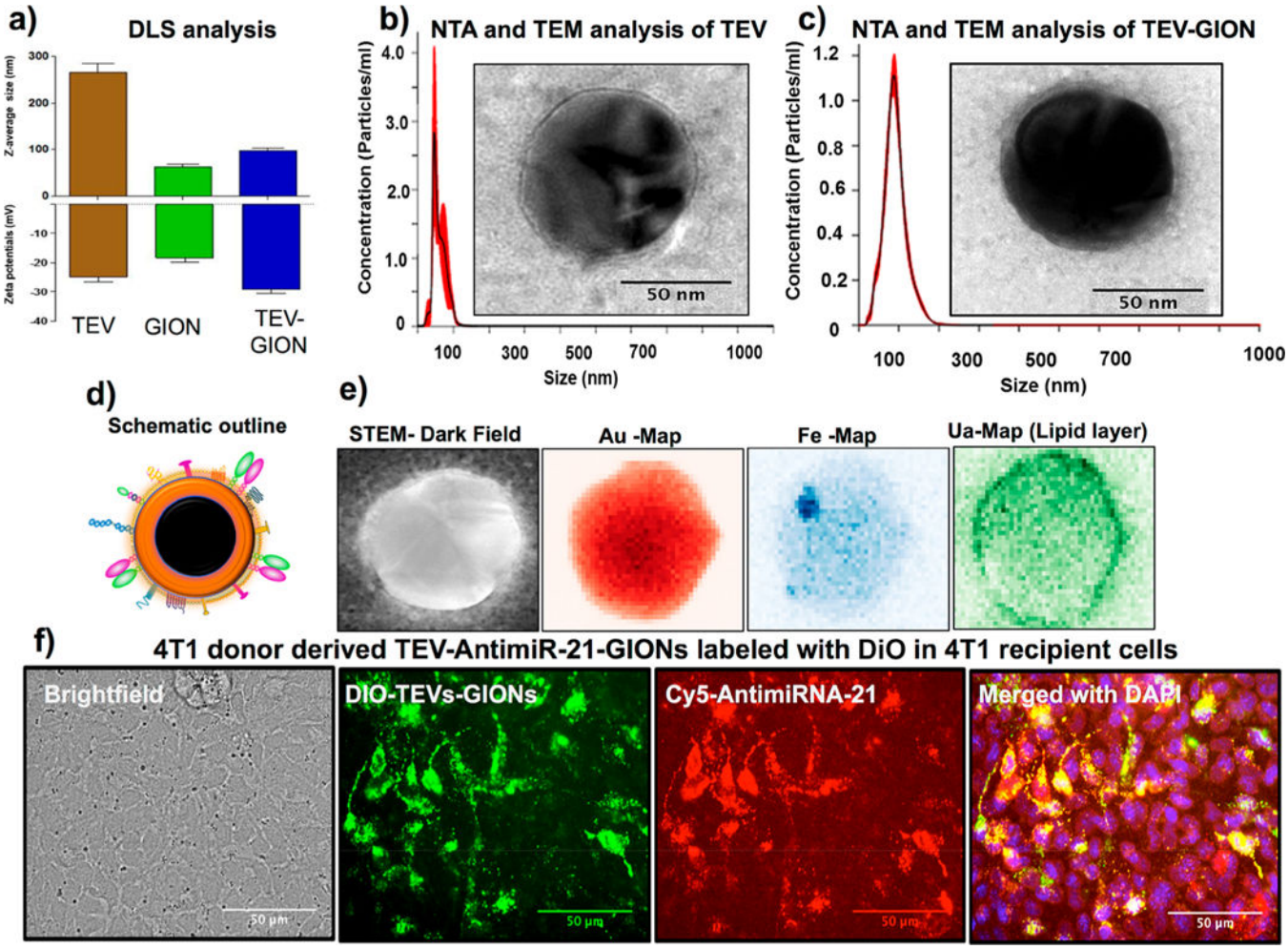

Figure 4.

Characterization of TEV-coated gold−iron oxide nanoparticles for anti-miR-21 delivery and theranostic imaging. (a) Size and surface charge (ζ potential) of TEVs (brown), GIONs (green), and TEV-GIONs (blue); (b) size distribution (nanoparticle-tracking analysis) and transmission electron microscopy image of GIONs; (c) size distribution (nanoparticle-tracking analysis) and transmission electron microscopy image of TEV-GIONs; (d) schematic outline shows theTEV-GIONsshape; (e)STEM−EDXresults show the hybrid bimetallic core of gold−iron oxide, wrapped by the tumor-cell-derived extracellular vesicles (lipid layer); and (f) transfection of donor 4T1-derived EV (labeled with DiO) coated GION-Cy5-anti-miR-21 delivery in 4T1 recipient cancer cells.

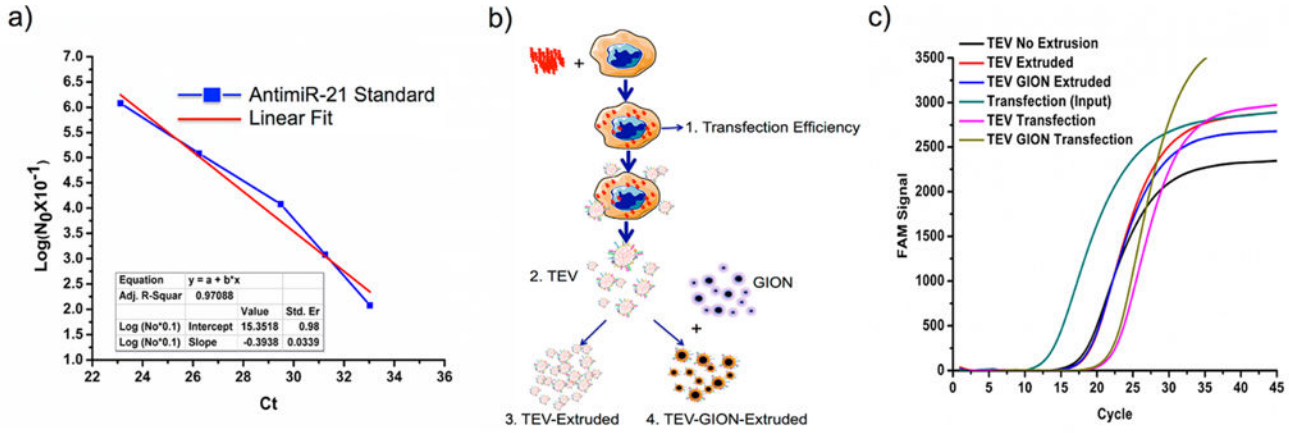

d)

	Mean Ct	Log(Nox 0.1)	Copy Number	Dilution factor	Total copy number	Transfected AntimiR-21	Transfection efficiency
Quantification of AntimiR-21 transfection in 4T1 cells						**pmol**	
Transfection	14.11500	9.7916	6.16595E10	75x50=3750	2.312231E14	385.37	77.074%
Quantification of EV loaded AntimiR-21						**Total EV**	**AntimiR-21/ EV**
TEV	19.32922	7.7382	5.4701596E8	20x5x7.5x3= 2250	1.230785E12	1.2E10	102.5
TEV-Extruded	19.45195	7.66017	4.5708818E8	20x5x7.5x3= 2250	1.028448E12	1.12E10	91.82
TEV GION-Extruded	19.45728	7.66227	4.5919801E8	20x5x7.5x3= 2250	1.331955E12	1.12E10	118.91
Quantification of AntimiR-21 loaded EV transfection						**Input AntimiR-21**	**Transfection efficiency**
TEV	21.30683	6.9593	8.9125E7	143x5=715	6.3724E10	2.9015E11	21.96%
TEV GION	18.7837	7.397	2.494594E8	73.3x5=366	9.1302E10	3.7575E11	24.29%

Figure 5.

Evaluation of anti-miR-21 transfection and loading efficiencies in transfected 4T1 cells, TEVs isolated from 4T1 cells, TEVs after extrusion with and without GIONs, and from 4T1 transfected with TEVs and TEV-GIONs as absolute copy numbers. (a) Standard plot of antimiR-21 in different copy numbers and the corresponding fitting curve derived by gene specific qRT-PCR amplification. (b) Schematic illustration explaining different stages of the procedure in which anti-miR-21 copy numbers were quantified for evaluation. (c) qRT-PCR analysis showing the amplification efficiency of anti-miR-21 isolated at different stages of TEVs processing. (d)A summarized table showing the quantitative values of the absolute number of copies of anti-miR-21 estimated in TEVs and TEV-GIONs at different stages of their evaluation.

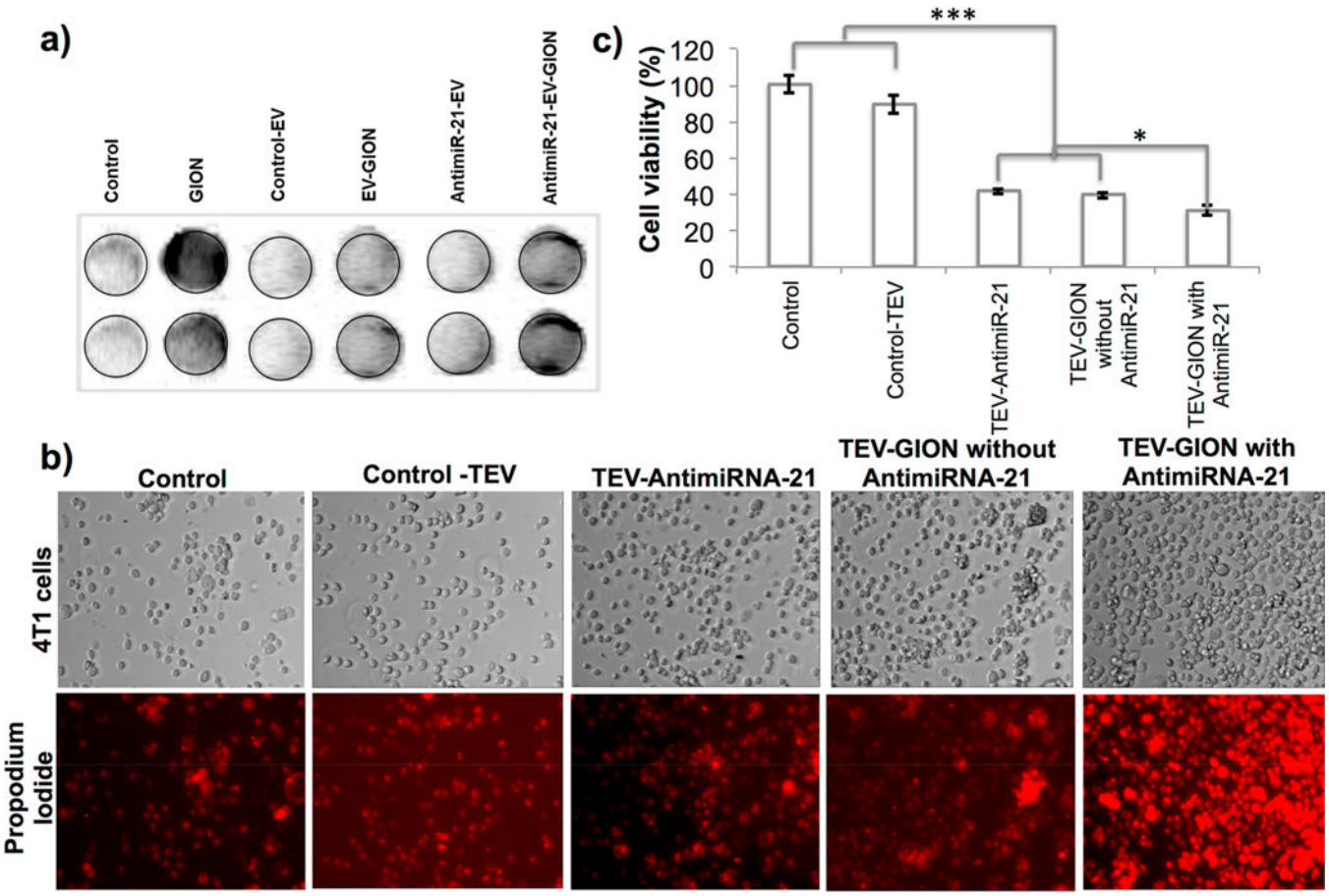

Figure 6.

Characterization of nanotheranostic properties of TEVs-GIONs. (a) *In vitro* MR imaging of 4T1 cells 24 h after the delivery of TEV-anti-miR-21-GIONs. (b) Photothermal therapy evaluated in 4T1 cells after the delivery of TEV and TEV-anti-miR-21-GIONs for 24 h and treated with 5mW980 nmNIR light (Hotstuff 3 V 980nm 5mW adjustable focusable infrared laser diode) for 15 min and assessed for therapeutic effect by propidium iodide staining based fluorescent microscopy assay. (c) Photothermal therapy evaluated in 4T1 cells after the delivery of TEVs, TEV-anti-miR-21, TEV-GIONs, and TEV-anti-miR-21-GIONs for 24 h and treated with a 5mW980 nm NIR light (Hotstuff 3 V 980 nm 5 mW adjustable focusable infrared laser diode) for 30 min and assessed for therapeutic effect after 48 h by cell titer blue assay (single asterisks indicate $p < 0.5$, and triple asterisks indicate $p < 0.001$).

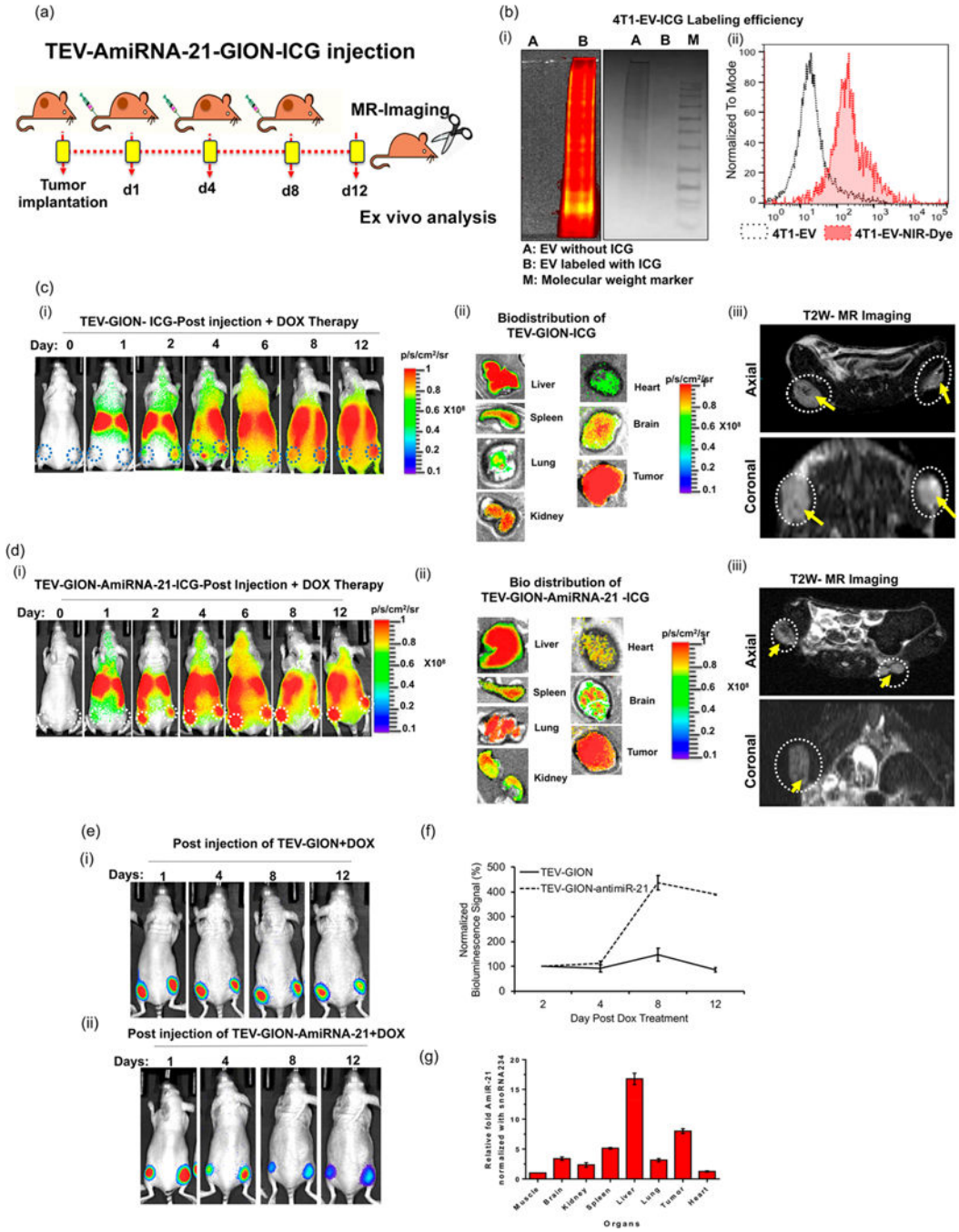

Figure 7.

In vivo biodistribution and anti-tumor properties of TEV-GIONs and TEV-GIONs-anti-miR-21 in combination with DOX. (a) Schematic outline shows the *in vivo* experimental design for treatments and imaging timelines. (b) 4T1-TEV-ICG labeling efficiency: (i) ICG-labeled TEVs after resolved in SDS-PAGE−IVIS imaging (left) and Coomassie blue staining (right) and (ii) FACS analysis of Alexa649-labeled TEVs. (c) (i) NIR fluorescence imaging of animals at 0, 1, 2, 4, 6, 8, and 12 days post-injection with three consecutive doses of TEV-GIONs-ICG, (ii) *ex vivo* fluorescence imaging of major organs (liver, spleen, lung, heart,

brain, kidney, and tumor) collected from animals 12 day after injection with TEV-GION-ICG, and (iii) T2WMRimaging of TEV-GION-ICG-treated animals [the negative contrast of GION is highlighted with arrow mark in tumor (circle)]. (d) (i) NIR fluorescence imaging of animals at 0, 1, 2, 4, 6, 8, and 12 days post-injection with three consecutive doses of TEV-anti-miR-21-GIONs-ICG, (ii) *ex vivo* fluorescence imaging of major organs (liver, spleen, lung, heart, brain, kidney, and tumor) collected from animals 12 day after injection with TEV-anti-miR-21-GIONs-ICG, and (iii) T2W MR imaging of TEV-anti-miR-21-GIONs-ICG-treated animals (the negative contrast of GIONs is highlighted with arrow marks in the tumor (circled in the image); (e) (i, ii) *In vivo* bioluminescence imaging for the growth of xenografts of 4T1-Fluc-eGFP cells implanted in nude mice (top and bottom rows show the bioluminescence images of animals that received TEV-GIONs-ICG and TEV-anti-miR-21-GION-ICG plus DOX, respectively, at days 1, 4, 8, and 12); (f) quantitative graph showing the change in the bioluminescence signal from animals that received TEV-GIONs-ICG and TEV-anti-miR-21-GIONs-ICG plus DOX treatment; (g) biodistribution of anti-miR-21 in different organs of animals that received TEV-anti-miR-21-GION 12 days after treatment with 3 consecutive doses (days 1, 4, and 8).

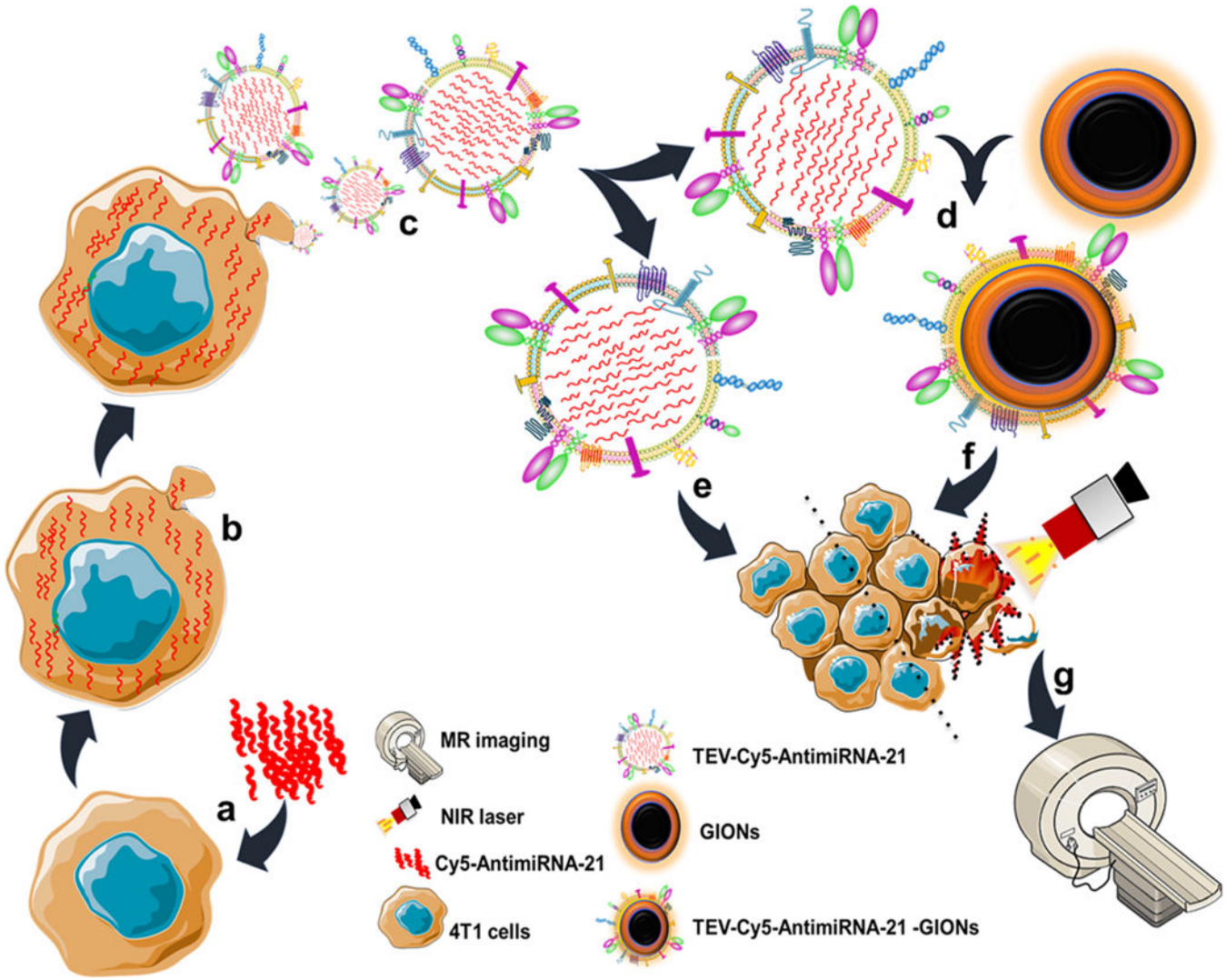

Scheme 1.

Schematic Illustration of the Preparation of TEVs-Cy5-anti-miRNA-21 and TEVs-Cy5-anti-miRNA-21-Coated Gold Iron Oxide Nanotheranostics[a] [a](a) Transfection of Cy5-anti-miRNA-21 into the donor 4T1 cells, (b) Cy5-anti-miRNA-21-packed donor 4T1 cells, (c) production of4T1 tumor cell derived extracellular vesicles *in situ* loaded with Cy5-anti-miRNA-21, (d) the production of TEVs-Cy5-anti-miRNA-21-coated GIONs by the top-down fabrication process, (e) TEVs-Cy5-anti-miRNA-21-mediated cancer therapy, (f) TEVs-Cy5-anti-miRNA-21-GIONs-mediated multimodal imaging and photothermal cancer therapy, and (g) MR imaging of 4T1 cancer cells delivered by TEVs-Cy5-anti-miRNA-21-GIONs.